

The Effects of Fluid Pre-Conditioning on the Deformational Response of a Laboratory Fault

Patrick Bianchi^{a,*}, Paul Antony Selvadurai^a, Antonio Felipe Salazar Vásquez^{a,b}, Claudio Madonna^c, Stefan Wiemer^a

^aSwiss Seismological Service, ETH Zurich ^bInstitut für Bau und Umwelt, Eastern Switzerland University of Applied Sciences

^cDepartment of Earth and Planetary Sciences, ETH Zurich *Corresponding author: patrick.bianchi@sed.ethz.ch

Peer review status:

This is a non-peer-reviewed preprint submitted to EarthArXiv. We have also submitted a preprint to Earth and Planetary Sciences for peer review.

The Effects of Fluid Pre-Conditioning on the Deformational Response of a Laboratory Fault

Patrick Bianchi^{a,d}, Paul Antony Selvadurai^a, Antonio Felipe Salazar Vásquez^{a,b}, Claudio Madonna^c, Stefan Wiemer^a

^aSwiss Seismological Service, ETH Zurich, Sonneggstrasse 5, Zurich, 8092, Switzerland
^bInstitut für Bau und Umwelt, Eastern Switzerland University of Applied
Sciences, Oberseestrasse 10, Rapperswil, 8640, Switzerland
^cDepartment of Earth and Planetary Sciences, ETH Zurich, Sonneggstrasse
5, Zurich, 8092, Switzerland
^dCorresponding author: patrick.bianchi@sed.ethz.ch,

Abstract

We investigate the effects of fluid pre-conditioning on the deformational response of a critically stressed laboratory fault. We employ distributed strain sensing with optical fibers to track fault-parallel and axial deformation during six reactivation tests via fluid injection that were performed on a sawcut cylindrical sample of Rotondo granite confined at 20 MPa. The strain measurements are complemented by the active and passive use of sixteen piezo-electric transducers, which allows us to track P-wave velocity variations associated with fluid movement along the fault and to detect acoustic emissions. By relying on the fault-parallel distributed strain measurements, our results show that fluid pre-conditioning promotes the development of strain heterogeneities along the fault due to channelized fluid flow. The distributed strain sensing technology effectively detects the role of aseismic slip in promoting a more uniform stress distribution and smoother slip propagation across larger fault segments in the fluid pre-conditioned tests. Conversely, rapid fluid pressurization in not pre-conditioned faults prevents smoothing of shear resistance heterogeneities, leading to the formation of barriers that can cause foreshocks and overall less predictable dynamics. Our findings are promising and provide novel insights that may help better understand the dynamics controlling fluid-induced fault instability and rupture nucleation and design injection protocols based on fluid pre-conditioning in order to reduce the risk of induced seismicity.

1. Introduction

Renewable energies have become increasingly essential in addressing the global challenges related to climate changes and energy security. Among several technologies that could play a crucial role in the transition towards zero-emission energy targets, enhanced geothermal systems (EGS) hold significant promise (e.g., Scheck-Wenderoth et al., 2013). EGS aim to exploit the heat stored in high-temperature formations, which are typically found at depths of ~ 3 kilometers or deeper. To create a geothermal reservoir at such depths, highly-pressurized fluids are injected to enhance the permeability of a rock formation by hydraulic fracturing or by reactivating pre-existing fractures (Villiger et al., 2020). This procedure is known as hydraulic stimulation (e.g., Zimmermann and Reinicke, 2010). Hydraulic stimulation, however, has often been regarded as the cause of damaging, induced earthquakes, a phenomenon known as induced seismicity (Moein et al., 2023, and references therein). Induced earthquakes have caused the abandonment of many geothermal projects (Deichmann and Giardini, 2009; Grigoli et al., 2018), which has lead to substantial economical losses and the undermining of the societal acceptance of such projects (Mignan et al., 2015; Trutnevyte and Wiemer, 2017). Despite significant, recent advances, we still lack a fundamental understanding of the physical mechanisms controlling the occurrence of induced seismicity, which limits the possibility of widely employing this technology.

In response to the injection of highly-pressurized fluids in the subsurface, the stress state of faults can be perturbed, which leads to fault reactivation and potentially triggering of dynamic instabilities along critically stressed fractures (Hubbert and Rubey, 1959). Several mechanisms are believed to control the occurrence of induced seismicity: pore-pressure diffusion, aseismic premonitory slip, poro-elastic coupling and thermo-elastic stress perturbations are considered to be primary triggering mechanisms, but more may exist (Moein et al., 2023).

Pore-pressure diffusion has been identified as an important triggering mechanism for induced events in the specific case of EGS stimulations. When the highly-pressurized fluids flow through pre-existing fractures and faults, their effective normal stress is decreased, leading to a reduction of the fault strength (Hubbert and Rubey, 1959). This was mathematically expressed as:

$$\tau = \mu \cdot \sigma_N' + C,\tag{1}$$

where

$$\sigma_N' = \sigma_N - \alpha \cdot p_f, \tag{2}$$

is the effective stress (Terzaghi, 1936), σ_N the normal stress, p_f the pore-pressure, τ the shear stress at failure, α the Biot's coefficient, μ the friction coefficient and C the cohesion. A critical parameter for pore-pressure diffusion is permeability, which controls the velocity with which fluids flow but also controls the pressurized zone on the faults (Cappa et al., 2018). Permeability heterogeneities along a fault may be caused by different reasons, such as a heterogeneous distribution of asperities (Dieterich and Kilgore, 1994; Selvadurai and Glaser, 2017) or the presence of gouge (Zimmerman et al., 1992; Wang et al., 2024). Roughness has been shown to regulate the hydraulic and mechanical aperture of fractures, thus influencing the fluid flow along them (Pyrak-Nolte and Nolte, 2016; Vogler et al., 2018; Rezaei Niya and Selvadurai, 2019; Huo et al., 2024). Since fluids preferentially flow through highly permeable paths, permeability heterogeneities may favor channelized flow, which would enhance a heterogeneous deformation response along faults (Bense et al., 2013; Vogler et al., 2018; Wenning et al., 2021; Huo et al., 2024).

Slip along faults has also been observed to occur as eismically and has been recognized to be a significant trigger mechanism of induced seismicity (e.g., Galis et al., 2017). Local failure initiates once the condition in Eq. 1 is satisfied and is realized as slip on thin, planar discontinuities. Slip dissipates energy in the system by reducing the shear stress on the fault plane. It can grow in a stable manner, producing a patch that expands outward in a quasistable fashion (e.g., Ohnaka, 1992). If this slowly expanding region reaches a critical nucleation size, the system may transition into a dynamic slip event. The growth of the slipping region may be governed by slip (e.g., Ida, 1972; Ohnaka, 2003) or by rate-dependent constitutive laws (e.g., Dieterich, 1992). Whether a dynamic instability develops is theoretically determined by an energy balance between the potential strain energy stored in the surrounding rock mass and the work dissipated along the interface to propagate the slip (e.g., Rubin and Ampuero, 2005). The critical nucleation size is inversely proportional to the effective stress, which couples pore fluid pressure to the instability via Eq. 1, adding further complexity as fluid diffusion depends on fracture permeability (Garagash and Germanovich, 2012).

Aseismic slip may propagate faster than the pore-pressure front, enhancing the possibility of loading critically stressed faults at higher distances from the injection well (Garagash and Germanovich, 2012; Cebry and McLaskey, 2021). In this regard, (underground) laboratory experiments play a crucial role in advancing our understanding of the trigger mechanisms for induced seismicity. Experiments performed at the reservoir (Guglielmi et al., 2015; Villiger et al., 2020; Ma et al., 2022) and meter/centimeter (French et al., 2016; Scuderi and Collettini, 2018; Passelègue et al., 2018; Noël et al., 2019; Proctor et al., 2020; Cebry and McLaskey, 2021) laboratory scales have provided important insight into both seismic and aseismic processes governing fault reactivation caused by fluid injection.

Research efforts have investigated the influence of injection on the reactivation and arrest of pressurized faults (e.g., Segall and Rice, 1995; Garagash and Germanovich, 2012; Galis et al., 2017). Several studies have been conducted to highlight the impact of the injection rate (e.g., Passelègue et al., 2018; Wang et al., 2020), the injection pressure (e.g., Almakari et al., 2019) and the fluid pressurization rate (e.g., French et al., 2016; Wang et al., 2020, 2024) on the promotion of seismic slip along faults. Proctor et al. (2020) installed a pressure sensor on the fault interface and measured pressure variations dictated by the interplay of compression and dilation along the fault. However, the mechanics associated with fluid-structure interactions in fault zones remain complex and not well understood (Selvadurai and Selvadurai, 2025).

Experiments aimed at the reactivation of pre-existing faults at the reservoir scale (e.g., Guglielmi et al., 2015) have used fluid pre-conditioning as a potential injection technique that may help control and target the reactivation of specific faults. Injection strategies relying on fluid pre-conditioning include an initial phase, in which the fluid is injected at low pressures for prolonged time intervals before increasing it to the targeted maximum value. The prolonged pressurization during the initial phase is believed to condition a more permeable structure within the rock mass by: (i) bringing it closer to the Mohr-Coulomb failure envelope (Eqs. 1 and 2) and (ii) doing this over a larger region. The secondary phase of this experiment involves a sudden increase of injection pressure that perturbs the system providing a "kick" in fluid pressure from the injection site, also known as 'hydraulic hammer' (Moein et al., 2023). In theory, this kick stimulates the more permeable structure that has been pre-conditioned in two ways to promote failure. The mechanisms during the secondary phase are unclear but may be driven by

fluid-enhanced dilation (Segall and Rice, 1995; Cappa et al., 2019; Proctor et al., 2020; Selvadurai and Selvadurai, 2025), allowing the pressurization front to reach higher distances from the injection well along the targeted high permeability feature. Despite the interest in applying similar injection strategies in geoenergy-related applications, the mechanisms controlling these phenomena need more investigation.

Here, we use state-of-the-art technologies to monitor the effects of fluid pre-conditioning on the deformational response of a critically stressed, saw-cut Rotondo granite sample confined at 20 MPa. Six reactivation tests and their associated stick-slip events are examined: three with initial fluid pre-conditioning and three without. A combination of DSS with optical fibers and piezo-electric transducers (PZT) measures total deformation, detects acoustic emissions (AEs), and tracks P-wave velocity variations linked to fluid diffusion along the fault surface. This monitoring approach enables us to investigate preseismic deformation mechanisms and highlight differences caused by fluid pre-conditioning compared to monotonic injection protocols.

2. Material and Methods

2.1. Sample Lithology and Preparation

The tests are performed using a cylindrical sample of Rotondo granite (Fig. 1a) that was extracted from the Bedretto Underground Laboratory for Geosciences and Geoenergies (Bedretto Lab, Switzerland), where different geothermal and fault reactivation experiments are performed at the hectometer scale (e.g., Ma et al., 2022). This lithology has the following mineralogical composition: quartz (25-35%), K-feldspar (20-40%), plagioclase (10-25%) and biotite (3-8%) (Rast et al., 2022, and references therein). The sample density equals approximately 2600 kg/m³, the Young's modulus is ~50 GPa and the Poisson's ratio equals 0.26-0.31 (David et al., 2020; Salazar Vásquez et al., 2024). Past investigations of the wave velocities of Rotondo granite at zero-confinement conditions indicate that the P-wave velocities range between 3500 m/s and 5500 m/s for dry and saturated samples, respectively (David et al., 2020). During a triaxial deformation test with a confining pressure of 10 MPa, the P-wave velocity in dry conditions was found to be 4600 m/s (Salazar Vásquez et al., 2024).

The sample is saw-cut with an angle $\phi = 35^{\circ}$ from the central axis of the sample (Figs. 1a and b) with a height of 144.5 mm and a diameter of 74.6 mm. We refer to the two sample halves as foot wall (FW) and

hanging wall (HW) for the bottom and top halves, respectively. Two vertical boreholes with a diameter of 5 mm are drilled from each end surface to the sample fault (Figs. 1a and b). The borehole in the FW is employed as the injection borehole, whereas the one in the HW as the extraction borehole. The fault surfaces are treated with a hand-lapping procedure with a 1200-grit diamond disc. This imposed a roughness on the surfaces and homogenized the imperfections left by the saw-cutting procedure, following the standard procedure used in other experiments with similar configurations (e.g., Ye and Ghassemi, 2018). The sample is inserted in a viton jacket during each experiment to isolate it from the confining oil.

2.2. Laboratory Facility and Monitoring Technologies

This study was carried out at the Rock Physics and Mechanics Laboratory of ETH Zurich (Switzerland). The experiments were performed using the LabQuake apparatus, a conventional triaxial machine equipped with state-of-the-art sensing capabilities. These include linear variable differential transformers (LVDTs) to monitor total axial deformation of the sample, DSS with fiber optics (Salazar Vásquez et al., 2022) and fully-calibrated, in-house developed PZTs for the detection of AEs (Selvadurai et al., 2022). A syringe-pump is used to inject fluids into the sample. The stiffness of the triaxial machine was determined through calibration tests over a range of confining pressure 5-160 MPa (Rast et al., 2024).

2.2.1. Point and Distributed Strain Sensing

Axial displacement is measured with a sampling frequency of 1 Hz using an axial LVDT mounted between the lower and upper steel pedestals that were in contact with the sample inside the cell. This allows us to determine the macroscopic total axial strain over the full sample height. Additionally, we perform DSS with optical fibers. DSS measurements are retrieved using a LUNA ODiSI 6104 interrogator with two active channels, one for each fiber mounted to the FW and HW. With this technology, we measure strain along the fibers with a sampling frequency of 40 Hz and a spatial resolution of 2.6 mm. For a thorough description of the details regarding the application of this sensing technology in a triaxial machine, the reader should consult Salazar Vásquez et al. (2022).

Dry failure envelope and permeability tests were initially performed to better characterize the sample fault (see the Supplementary Material 1,2 and 3 for more details). For practicality, we did not to install the fibers for

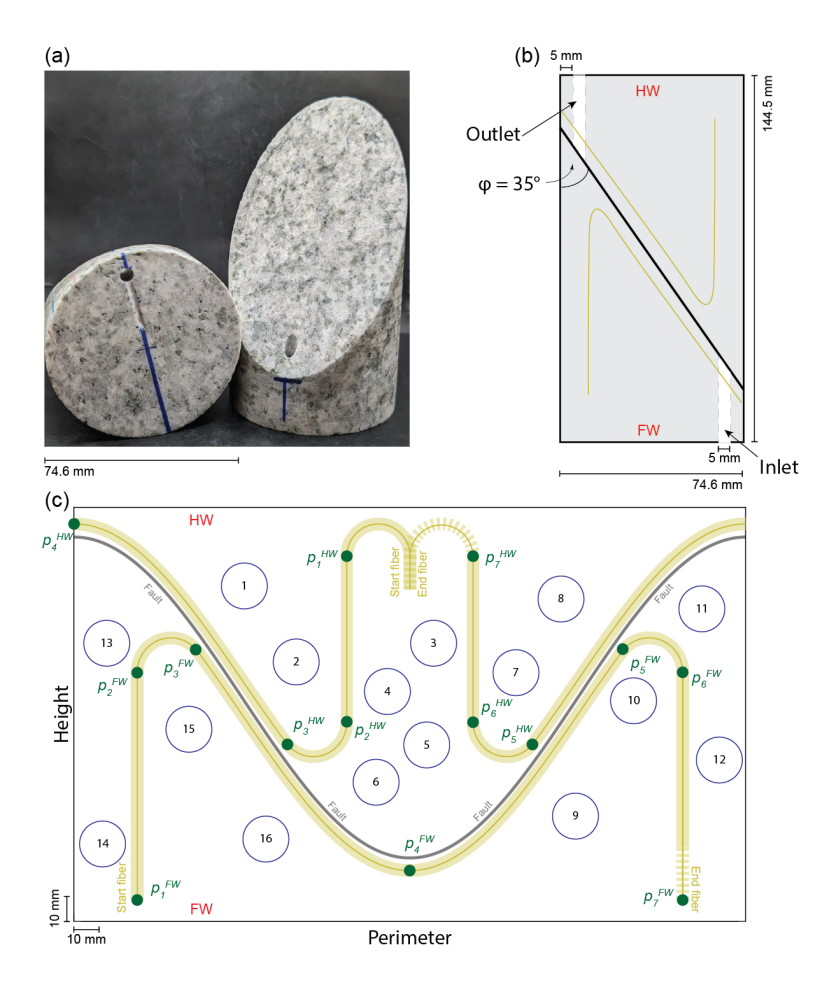


Figure 1: (a) A photograph of the two sample halves (HW on the left and FW on the right). (b) A schematic of the sample setup with the approximate positions of the DSS sensors and the two boreholes. (c) Projection of the PZT (black circles, numbered 1-16) and DSS sensor positions on the sample surface. The segment points of the fiber cables are indicated as P_1^{FW} - P_7^{FW} for the FW and P_1^{HW} - P_7^{HW} for the HW.

these tests to avoid damaging them before the fluid reactivation tests. When implemented, two polymide-coated fibers are installed on the sample surface (i.e., one for each sample half) following the schematic shown in Fig. 1c (setup adapted from Rast et al., 2024). These are glued using a cold-curing instant adhesive (Ergo 5011 Universal) while manually pre-tensioning them. To protect these during the experimental preparation and to improve the coupling between them and the rock surface (Salazar Vásquez et al., 2022), we further apply a coating of two-part epoxy (ZAP Z-Poxy). Following the

schematic depicted in Fig. 1c, each fiber results in three distinct segments: two axial $(P_1 \to P_2, P_6 \to P_7)$ and one fault-parallel $(P_3 \to P_5)$ segments, which measure axial and fault-parallel strain, respectively. The fault-parallel segment is glued at approximately 4 mm from the fault. The curved segments $(P_2 \to P_3 \text{ and } P_5 \to P_6)$ are only designed to position the fibers in the correct direction for the segments of interest and the strain measurements retrieved along these curved portions are neglected in this study. Segment points of the HW and FW are respectively differentiated as $P_1^{HW} \to P_7^{HW}$ and $P_1^{FW} \to P_7^{FW}$, whereas $P_1 \to P_7$ refers to both sample ends, simultaneously. Strain measurements are tared at the start of each fluid reactivation test (see test protocols in Section 2.4), thus providing information regarding the relative deformation induced by the injection. To address technical noise issues in the DSS measurements (e.g., sudden spikes or missing data), the affected sections are corrected by linearly interpolating in time between the preceding and subsequent data samples from the same fiber gauge. The time synchronization between DSS measurements and the macroscopic data is adjusted, aligning the data sets with respect to the start of the axial stress increase towards the critical stress state during each reactivation test (Rast et al., 2024). We follow the convention with (relative) compression and (relative) extension being positive and negative, respectively.

2.2.2. Acoustic Emission Monitoring System

We detect AEs by employing 16 conical-type PZTs, which were designed in-house to resist high pressures and temperatures (Selvadurai et al., 2022). These are used for both passive monitoring and ultrasonic surveying with the LabQuake apparatus (e.g., Bianchi et al., 2024; Salazar Vásquez et al., 2024). Sixteen portholes are punched to install the sensors in contact with the sample surface. To avoid oil leaks within the jacket, the portholes are covered with a two-part epoxy (LOCTITE® EA 9455). Figure 1c shows a schematic of the unwrapped locations of the PZTs with respect to the sample and the fault. During the fluid reactivation tests, we record AEs using a data acquisition system (TraNET EPC-TPCE, Elsys AG) in a triggered mode with a sampling frequency of 20 MHz. Each time the system is triggered, signals from 16 PZTs are saved in a block of 20 milliseconds (± 10 milliseconds from the triggered sample). The signals are not amplified and are digitized in the range \pm 0.05 V. The trigger threshold is set in window out mode at a voltage slightly above the background noise level. Wave arrivals are manually picked and AEs are located by minimizing the L²-norm of a cost function (Bianchi

et al., 2022) and by assuming an homogeneous model with P-wave velocity $\sim 6300 \text{ m/s}$ (David et al., 2020) for fluid-saturated Rotondo granite confined at 20 MPa, which is the same confining pressure applied during the fluid reactivation tests. However, the sample used here was not pre-saturated, as the aim was to investigate fault reactivation from an initially dry state of it.

2.3. Ultrasonic Surveys During Fault Flooding

To investigate how the injected water diffuses through the fault, we perform ultrasonic surveys during the initial fault flooding (i.e., injection from dry conditions) phase of a separate set of reactivation tests performed. Due to technical issues encountered in a later stage of this set of tests, we have only presented the data related to the flooding phase. After having confined the sample and having vacuumed it for approximately 30 minutes, we inject water for 30 minutes with a step-wise increase of the inlet pressure to a maximum of 4 MPa in hydrostatic conditions (see Fig. 4a for the injection protocol). During this phase, we perform ultrasonic surveys to track P-wave velocity variations along the fault. The PZT sensors in contact with the FW (PZTs 9-16, Fig. 1c) are used to repeatedly produce 350 V pulses using a high-voltage multiplexer unit (HVP, AE-HV-MUX, Elsys AG), which generates pulses with a Piezosystem Jena voltage amplifier (HVP 1000/200) (Selvadurai et al., 2022).

The PZT sensors installed in the HW (PZTs 1-8, Fig. 2c) are employed as receivers. The recorded waveforms are stacked (10 pulses) to increase the signal-to-noise ratio after being aligned by using the crosstalk signal on each channel (Bianchi et al., 2024). The wave arrivals are then picked with higher accuracy using the Akaike-Information-Criterion algorithm (Akaike, 1974). Examples of the picking of the arrivals are provided in the Supplementary Material 4 (Fig. S2).

By tracing each source-receiver ray path, we compute the intersection points of the elliptical fault plane and the euclidean distance between sensor-receiver pairs. We then assign a P-wave velocity value to each of these intersection points by dividing the computed distance by the measured travel time. By interpolating the values on the intersection points with the Matlab function griddata, we create an interpolated map of velocity variations on the fault surface. We use the interpolation scheme v4, which is a biharmonic spline interpolation method. In the Supplementary Material 5, we provide the same fault velocity map formed with different interpolation schemes to show that the results found are independent of the chosen scheme.

2.4. Protocol of the Fluid Reactivation Tests

We perform six fluid reactivation tests at room temperature and at a constant confining pressure of 20 MPa. Tap water is used as the injection fluid and tests are performed under undrained conditions. After having reached the target confining pressure and before the first reactivation test, the fluid pressure pipes and the sample pore space are vacuumed for approximately 30 minutes to ease the sample saturation. The sample is successively flooded with water pressurized at 2 MPa for approximately 15 minutes. While holding the inlet pressure constant at 2 MPa, the sample is axially loaded with a constant displacement velocity of 1 μ m/s to achieve a critical stress state that corresponds to the 80% of the fault shear strength (Ji et al., 2022). Based on the determination of the dry failure envelope performed (see the Supplementary Material 2 for more details), we find $\tau_{80\%} \simeq 22$ MPa, which results in an axial stress of approximately 68 MPa. As soon as the critical stress state is reached, the piston position is held constant and, after 10 minutes, the injection protocols are initiated with a near-instantaneous inlet pressure increase at the targeted injection pressure. The fluid pre-conditioning (P-C) phases in Test 2, Test 5 and Test 6 last 10 minutes. After each stick-slip event, the inlet pressure is decreased to 2 MPa and the same steps listed above are followed to bring the fault back to the same initial, critical stress conditions. Details regarding the protocols used in each of the six tests are provided in Table 1 and Fig. 2, whereas a general overview of the whole experimental protocol is provided in the Supplementary Material 6.

3. Results

3.1. Mechanical Monitoring of Fluid Reactivation

Macro-mechanical, fluid and acoustic properties measured during the six fluid reactivation tests are listed in Table 1 and partially visualized in Fig. 2, whereas Figs. 3a-f display the fault-parallel distributed strain measurements (for visualization purposes, only one of ten measurements is shown) between points P_3 and P_5 (see Fig. 1c as a reference) for the FW (first column) and HW (second column) during the $Test\ 1$ to $Test\ 6$, respectively. The colorbars indicate the time in the tests and refer to the ones displayed in Figs. 2a-f. The light blue lines represent the measurements retrieved after the stick-slip events and provide insights on slip arrest. The measurements show heterogeneous distribution of strain immediately following injection.

Table 1: Properties of the six fluid reactivation tests. σ_N and τ are the applied normal and shear stresses, $P_{f,P-C}$ and $P_{f,kick}$ are the pre-conditioning and kick fluid pressures, respectively, Δvol_{inj} is the total injected volume from the start to the stick-slip event, $\Delta \tau$ is the strength drop, $\Delta S_{\text{tot}}^{**}$ is the total slip and $\Delta S_{\text{pre}}^{**}$ is the preslip. *Tentative P-C at 9 MPa but after approximately three minutes at this pressure, a stick-slip event is induced. **Estimated from the axial LVDT measurement.

	P- C	σ_N	au	$P_{f,P-C}$	$P_{f,\mathrm{kick}}$	Δvol_{inj}	Δau	$\Delta S_{\mathrm{tot}}^{**}$	$\Delta S_{\rm pre}^{**}$	foreshock
	[-]	[MPa]	[MPa]	[MPa]	[MPa]	[ml]	[MPa]	$[\mu m]$	$[\mu m]$	[-]
Test 1	no	35	22	n/a	18.0	2.5	1.7	30	3	yes
Test 2	yes	35	22	4.5	18.0	2.6	1.7	31	2	no
Test 3	no^*	35	22	n/a	9.0	1.2	1.6	31	3	no
Test 4	no	35	22	n/a	12.0	1.7	1.6	37	2	yes
Test 5	yes	35	22	3.0	12.0	1.7	1.6	38	3	no
Test 6	yes	35	22	6.0	12.0	1.8	1.4	33	3	no

The strain measured in the FW is generally of higher magnitude with respect to the HW. The prominent peaks of relative extension in the middle of the FW cable (close to point P_4^{FW} , Fig. 1c) are located at the closest point to the injection borehole and consistently show the higher extension in each test. The height of these peaks appears to scale proportionally with the final fluid pressure applied in each test.

The initial response to injection shows that fault-parallel measurements in both FW and HW fiber cables measured increasing relative extension with time everywhere along the array. Shortly (i.e., <5 to 10 seconds) before the stick-slip events, we observe fronts of relative compression in the FW at the sides of the cable segment (highlighted with green ellipses as example in Fig. 3a), close to the points P_3^{FW} and P_5^{FW} . At this moment in the HW, the propagation front is extensional and was also observed at the two ends of the segment $P_3^{HW} \to P_5^{HW}$ (highlighted with violet ellipses as example in Fig. 3a). This combined behaviour of relative compression-extension on the two sides of the fault was also observed in a past injection experiment with the same setup of the optical fibers (Rast et al., 2024).

After the stress drop due to the stick-slip events, the strain profiles (light blue lines in Fig. 3) of both sample halves show an immediate increase in relative extension except for the middle portion of the HW segment. In this half of the sample, the region closer to the extraction well (i.e., close to point P_4^{HW}) appears to be in a state of general compression after rupture arrest.

In the ideal case, with a perfectly homogeneous fault surface and sample, we would expect the left-hand side (i.e., $P_3 \to P_4$) and right-hand side (i.e.,

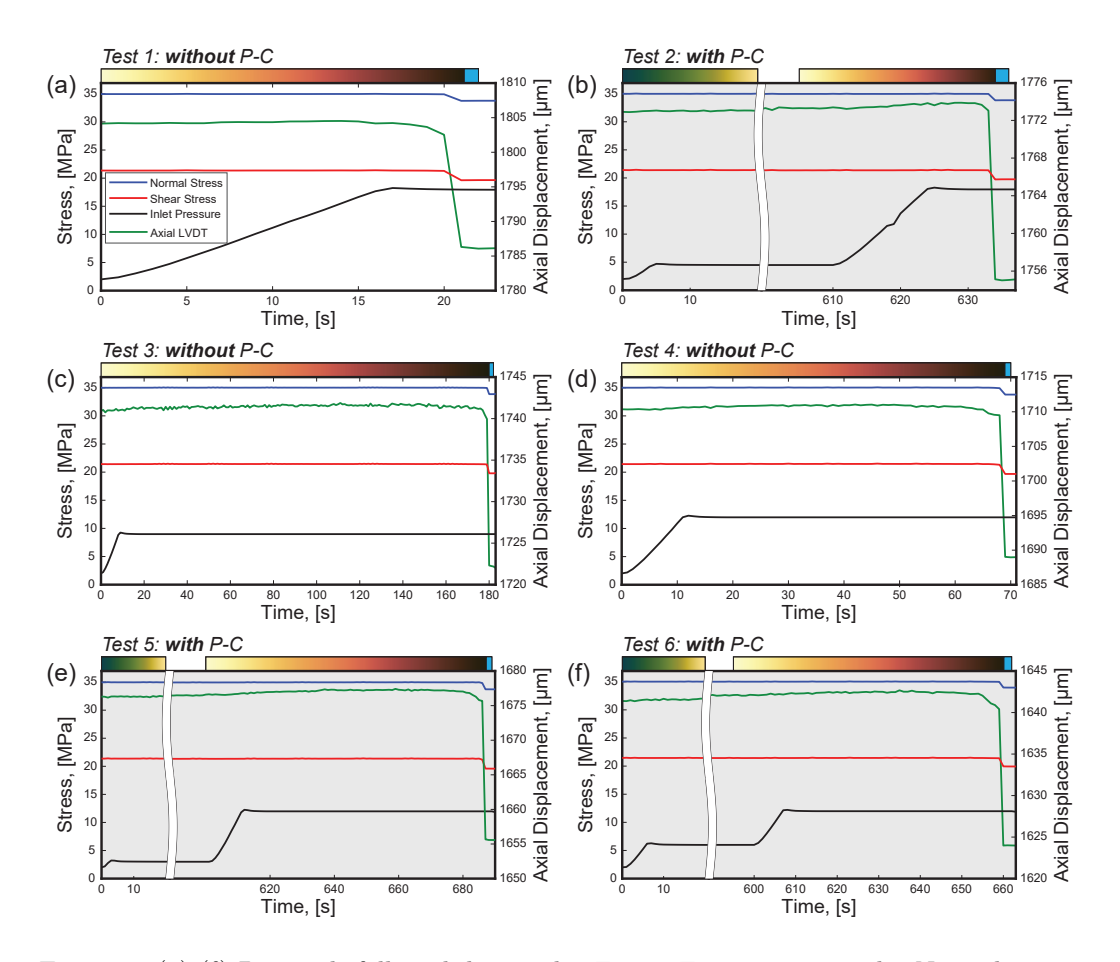


Figure 2: (a)-(f) Protocols followed during the $Test\ 1$ - $Test\ 6$, respectively. Normal stress (blue), shear stress (red), inlet pressure (black) and axial LVDT (green) as a function of time. The colorbars above the plots indicate the time in the test and are explained in the text. Tests involving fluid pre-conditioning (P-C) are indicated by a grey background.

 $P_4 \to P_5$) part of each fiber segment to respond symmetrically and deform equally in response to the fluid injection. However, this is not observed here, as strain heterogeneities are observed in fault-parallel strain arrays in the FW and HW. The strain measurements obtained from the left-hand side of the FW consistently indicate greater extension compared to the corresponding side of the HW in each test. Close to the extensional peaks in P_4^{FW} but directly on the right-hand side of them (indicated in Fig. 3b with a green arrow as example), we observe a region of the fault that generally appears to

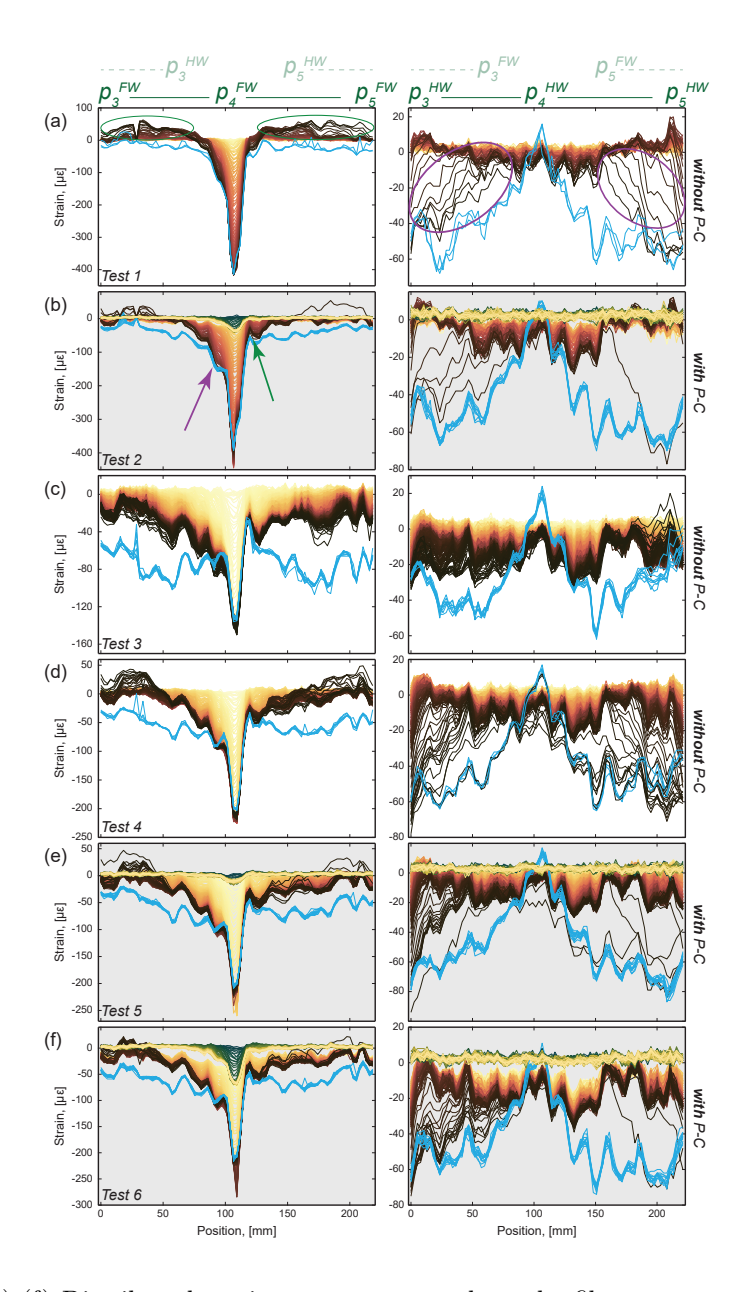


Figure 3: (a)-(f) Distributed strain measurements along the fiber segments $P_3 \rightarrow P_4 \rightarrow P_5$ for the FW (first column) and HW (second column) for the Test~1-Test~6, respectively. For visualization purposes, only one of ten measurements is visualized. The colorbars indicate the time in the specific test and refer to the ones displayed in Figs. 2a-f. Tests involving fluid pre-conditioning (P-C) are indicated by a grey background.

deform less than its symmetrical counterpart on the other side of the fault (indicated in Fig. 3b with a violet arrow as example). Differences between the fiber segment sides in the HW are also seen but are less pronounced. In the upper sample half, shortly before the stick-slip events, the fault region closer to P_3^{HW} generally display a stronger acceleration of deformation with respect to P_5^{HW} .

The reactivation tests performed after fluid pre-conditioning (Figs. 3b, e and f) display some differences if compared to the cases without the preconditioning (Figs. 3a, c and d), indicating a change in fault response to this injection strategy. During the ten minutes of pre-conditioning, the fault extends in the fault-parallel direction. This is observed in both the FWand HW strain measurements. As a consequence, when the inlet pressure is increased to its maximum, the stick-slip events are observed to occur at a slightly higher, average level of accumulated strain compared to the tests without pre-conditioning. Another distinction is found in the moments just prior to dynamic rupture (i.e., <5 to 10 seconds), where accelerated premonitory deformation is noted to accumulate in segments $P_3 \rightarrow P_4$ and P_4 $\rightarrow P_5$. In this time interval, the DSS measurements of the tests performed without pre-conditioning show accelerated deformation in both sides of the fault-parallel fiber segments and in both sample halves. Conversely, during the pre-conditioning tests only the left-hand side of the fiber segments $(P_3 \rightarrow$ P_4) experiences precursory, accelerated deformation, whereas we can detect only small precursory indications in the right side $(P_4 \rightarrow P_5)$.

A similar analysis has also been carried out with the distributed strain measurements retrieved along the four axial segments $(P_1 \to P_2, P_6 \to P_7)$. However, since the observations related to the effects of fluid pre-conditioning presented in the previous paragraphs are less apparent on the DSS axial arrays, we invite the reader to consult the Supplementary Material 7 for more details regarding these.

3.2. Local Variations in Ultrasonic Properties

We track P-wave velocity variations $\Delta V/V$ on the fault surface during the initial flooding phase (i.e., injection into a completely dry fault) for a set of injection tests performed under hydrostatic conditions. The P-wave velocity of Rotondo granite increases when saturated from an initial dry state (David et al., 2020). Therefore, we expect to observe relative increases in $\Delta V/V$ as the fluid diffuses along the fault from the injection borehole. Figure 4a shows the injection protocol followed during the flooding phase with the pink dots

b-g referring to the Figs. 4b-g, which depict the interpolated P-wave velocity variations determined on the fault surface. The colorbars are normalized with respect to the initial seismic velocity distribution V on the fault surface, which includes values that range between 4200 and 4800 m/s (Fig. 4b). The maximum seismic velocity variation detected is $\Delta V/V \sim +10\%$.

After approximately 500 seconds of injection and an increase of the inlet pressure to 1 MPa, we observe some patches of fluid that diffuse through the fault in the direction of the extraction borehole. However, the injected water does not diffuse in a straight line between the two boreholes. Until approximately 850 seconds of fluid injection, the left side of the fault appears to be more affected by the fluid front, showing higher increases in $\Delta V/V$ (Figs. 4c and d). This is consistent with the fault-parallel DSS measurements presented in Fig. 3, which show that in the left side of the fiber segments $(P_3 \to P_4)$ there is a higher degree of deformation with respect to the right side $(P_4 \to P_5)$. At later stages of the flooding phase (Figs. 4e-g), the fluid appears to spread more homogeneously across the fault. The patches of high seismic velocity initially observed grow in size and additional fluid paths and patches emerge on the right side of the fault. We note that the flooding phase lasts for approximately 30 minutes, while the fluid pre-conditioning injection performed during Test 2, Test 5 and Test 6 continues for only for 10 minutes (see Fig. 2).

4. Discussion

4.1. Channelized Fluid Flow in Rough Fractures

The fault-parallel DSS measurements presented in Fig. 3 show a heterogeneous deformation response of both sample halves to the injection of pressurized water. This asymmetric behavior, with differences mainly between the segments $P_3 \rightarrow P_4$ and $P_4 \rightarrow P_5$, suggests the presence of features that promote strain localization along specific portions of the fault. A likely cause is variations in fluid transport properties along the fault, controlled by heterogeneities in surface topography (Zimmerman et al., 1992; Ye and Ghassemi, 2018; Fang and Wu, 2022; Wang et al., 2024; Huo et al., 2024). The influence of topographic variability on channelized fluid flow under changing normal stress remains poorly understood, but it has been shown that increasing normal stress can enhance channelization in fractures with variable aperture (Pyrak-Nolte and Nolte, 2016). As confining stress increases

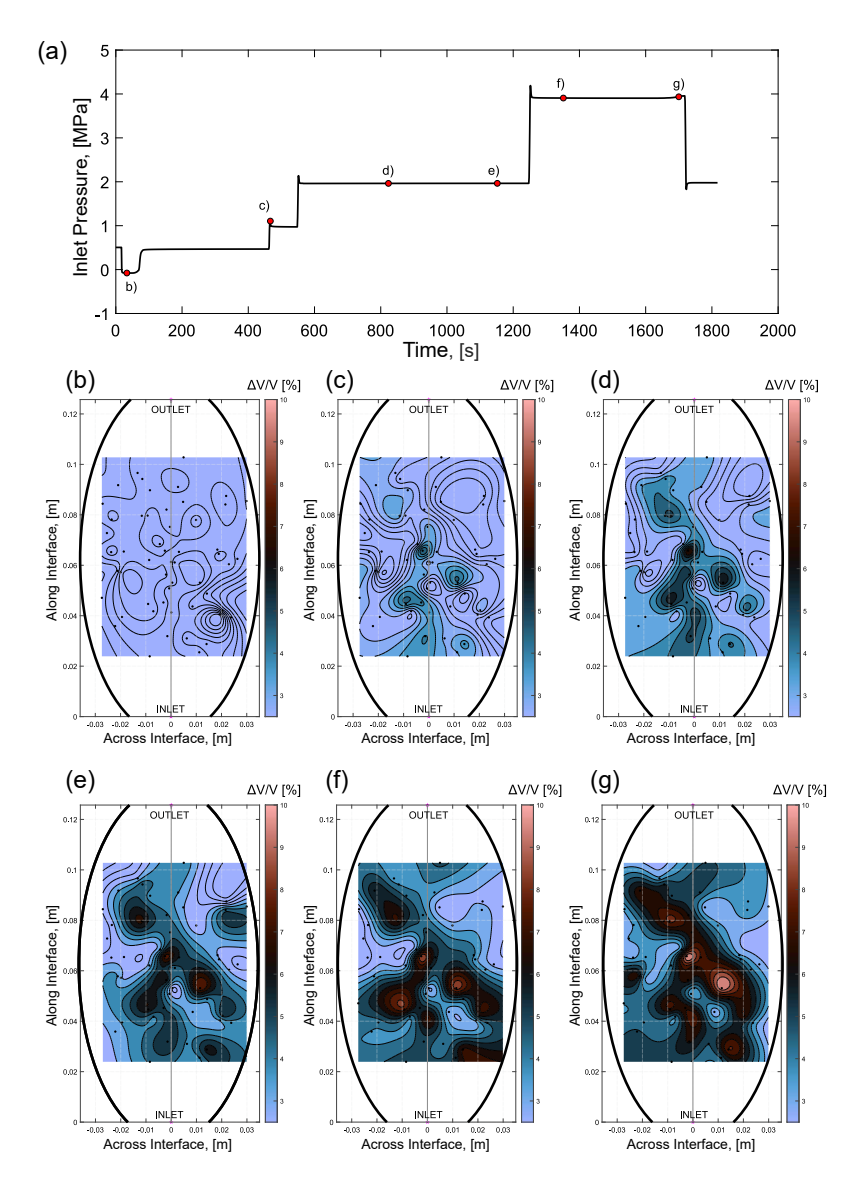


Figure 4: (a) The injection protocol followed during the flooding phase with the pink points b-g referring to the figures below. (b)-(g) The interpolated P-wave velocity variations $\Delta V/V$ determined on the fault surface. The black dots show the intersection points of the ray paths between sources and receivers, the pink stars at the bottom and top indicate the inlet and outlet locations, respectively, and the black curves are velocity isolines. The colorbars are normalized with respect to the initial seismic velocity distribution V on the fault surface.

and apertures gradually close, overall flow diminishes and becomes increasingly restricted to preferential flow paths (Rezaei Niya and Selvadurai, 2019; Huo et al., 2024). Before injection, the fault surface is locked under critical stress conditions, with regions of contact supported by asperities formed by the geometrical interaction of the two surfaces (Dieterich and Kilgore, 1994; Selvadurai and Glaser, 2015, 2017). Fault roughness has been shown to influence induced seismicity (Wang et al., 2024; Goebel et al., 2024) and has been linked to the overall strength of a fault, including its ability to resist both quasi-static and dynamic shear motion (see references in Selvadurai and Selvadurai, 2025).

At the onset of injection, pressurized fluid diffuses along the fault plane toward the trailing edge of the sample through higher wave velocity pathways identified by the ultrasonic surveys (Fig.4). We interpret such structures as consistent with the development of channelized fluid flow along the sample fault surface and we believe that they likely control the asymmetric deformational response observed in the DSS measurements (Fig. 3). Permeability heterogeneities and channelized fluid flow have previously been identified as key factors influencing fault reactivation in laboratory (Vogler et al., 2018; Wenning et al., 2021), numerical (Vogler et al., 2018), and field (Bense et al., 2013) studies of rough fractures. Pore-pressure increases within fault discontinuities may induce local dilation (Segall and Rice, 1995; Proctor et al., (2020). The fault-parallel DSS measurements (Fig.3) for both the FW and HW show several local variations of extension along $P_3 \rightarrow P_5$. Initially concentrated near the injection well, these features migrate upward along the fault over time. We interpret these extensional "bumps" as fluid-induced dilation occurring preferentially in certain zones due to channelization, rather than homogeneously along the interface. However, the complexity of these processes suggests that additional micromechanical mechanisms may contribute to the observed strain variations (e.g., Wang et al., 2020; Fang and Wu, 2022).

4.2. Dynamics of Fluid-Induced Fault Instability and Rupture Nucleation

Fluid reactivation can govern dynamic fault instability through multiple mechanisms, notably the interplay between aseismic weakening (Lui et al., 2021), elastic stress transfer (Wynants-Morel et al., 2020), and the reduction of effective stress via pressurized pore fluid migration within the fault zone (Proctor et al., 2020). The competition between these processes leads to

nuanced behaviors influenced by heterogeneity in fault structures. For example, permeability heterogeneities caused by near-fault fracture networks or roughness-induced channelized flow – concepts explored here – can significantly impact these dynamics. Such features are particularly important during the nucleation process within bounded fault regions, where slip can accelerate along thin, weakened discontinuities.

The ability of a fault surface to resist shear slip depends on various factors. Constitutive laws relating slip (e.g., Ohnaka, 2003) or slip-rate (e.g., Dieterich, 1979) to shear stress describe the shear-traction response relative to the fault resistance to rupture growth. Figure 5 summarizes the theoretical response for rupture nucleation on pre-existing weak discontinuities, originally proposed to explain laboratory observations (Ohnaka, 1992).

Model A (Fig. 5a) depicts a shear breakdown zone with a weaker region bounded by stronger areas with higher rupture resistance (orange profiles). A slip patch nucleates and propagates slowly outwards governed by its constitutive law, growing aseismically by consuming the elastic strain energy stored in the surrounding rock. Energy dissipation occurs as slip accommodates the reduction of shear stress. Once the nucleation patch, often referred to as the premonitory slip or preslip region, quasi-statically expands to reaches a critical size, dynamic rupture is triggered. This model has been extensively supported by laboratory experiments (e.g., Dieterich, 1979; Ohnaka and Shen, 1999; Selvadurai and Glaser, 2015; McLaskey, 2019) and numerical simulations (e.g., Dieterich, 1992; Cattania and Segall, 2021; Selvadurai et al., 2023; Wu and Barbot, 2025) with various constitutive laws. On the right side of Fig. 5a, shear stress and slip at two observation points are shown. The shear-traction response follows slip-weakening behavior: Point (1) corresponds to a location experiencing the passage of the slow (quasistatically) expanding rupture, while Point (2) depicts the response at a point experiencing the passage of the dynamic rupture.

Model B (Fig. 5b) illustrates rupture nucleation involving a local dynamic instability, or foreshock, which occurs prior to the mainshock. These localized instabilities, driven by heterogeneity in rupture resistance and fracture energy – often caused by micromechanical asperities formed during rough contact of fault surfaces (discussed in the previous section) – can influence the timing and location of the mainshock (Selvadurai et al., 2023; Noda et al., 2013). The right panels of Fig. 5b show the theoretical slip-weakening response at points near a local dynamic instability (Point (1)) and experiencing the passage of a dynamic rupture (Point (2)).

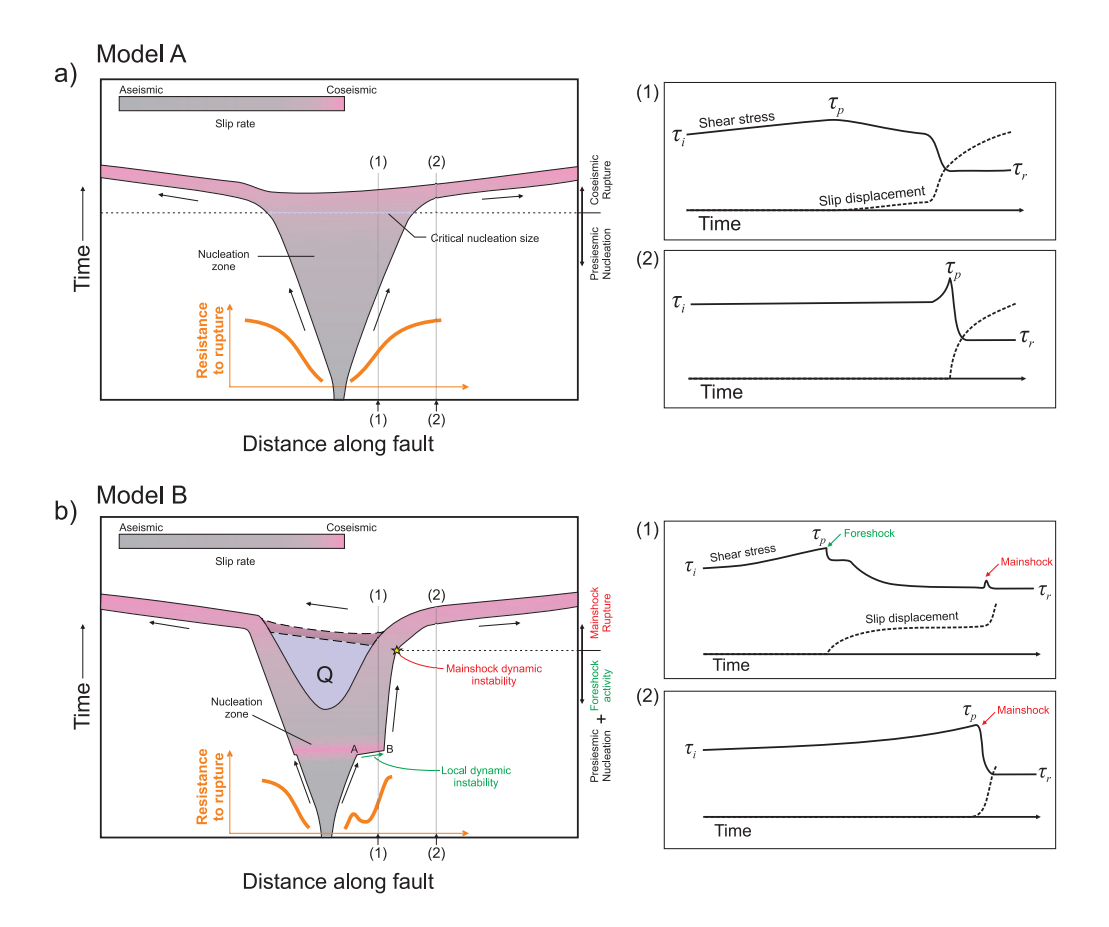


Figure 5: (a) $Model\ A$ represents the spatiotemporal expansion of a rupture along a thin discontinuity at a pre-existing interface, following the slip-weakening law. The shear resistance profiles are monotonically increasing, with slip initiating at the weakest point. (Right panel) Two observation points show the shear-traction response during (1) a slowly expanding rupture and (2) a dynamically propagating rupture. (b) $Model\ B$ illustrates rupture nucleation on a fault with variable resistance to rupture (orange profiles), which can lead to local instabilities (foreshocks) that complicate the nucleation process. Q denotes the region where shear stress has been reduced to a residual level. (Right panel) Responses at two points showing (1) behavior near a local foreshock and (2) the subsequent dynamic rupture propagation. Figure adapted after Ohnaka (1992).

For both models, we do not detail the slip-traction response at these observation points. Readers are referred to Ohnaka (1992) for a comprehensive explanation of the predicted slip-weakening behavior, which we use here to

hypothesize how fluid pre-conditioning influences the distribution of shear resistance (orange profiles) as inferred from strain responses in the fault-parallel DSS array.

4.3. Effects of Fluid Pre-Conditioning

4.3.1. Analysis of Fault Response With and Without Pre-Conditioning

We analyze the spatio-temporal responses from $Tests\ 6$ (pre-conditioning, Fig. 6a) and 4 (no pre-conditioning, Fig. 6b), approximately 10 seconds before the main shock-induced dynamic instability. Our focus is on specific portions of the DSS array, representing fault-parallel strain measured in the FW (red lines) and HW (black lines) at locations effectively spanning the same fault segment.

In the pre-conditioned case (Fig. 6a), responses strongly align with Model A (Fig. 5a). The sensors on the right array (orange box) exhibit a gradual, quasi-static increase in strain, characteristic of a slip front moving slowly – supporting the idea of aseismic slip and reduction of elastic strain energy. Conversely, the left array (green) shows a rapid acceleration to peak stress, consistent with a sudden rupture front passing through these points. This response aligns with Model A conceptual framework, where a weak zone undergoes aseismic slip that gradually consumes stored elastic energy before a critical threshold triggers a rapid dynamic rupture. These observations reinforce the idea that pre-conditioning fosters a predominantly aseismic nucleation phase on faults with an asymmetric response with smoother resistance to rupture, as predicted by the Model A.

In stark contrast, the not pre-conditioned scenario (Fig. 6b) displays a more complex behavior, best described by $Model\ B$. During this test, a fore-shock was detected via AE sensors (see Table 1), and evidence of it was observed in the dynamic strain measurements on the left side (purple region). Similarly, on the right side (pink array), the strain gradually increased, reached a peak, and then underwent a sudden drop – behavior predicted by $Model\ B$, where localized instabilities (foreshocks) induce rapid local stress drops and hasten the expansion of the nucleation zone. The shear stress in the aseismically slipping core region continues to decrease as the nucleation zone expands quasi-stably, eventually reaching a residual level within the slipweakening framework. This process creates the "quiescent" region marked by Q in Fig. 5b. The heterogeneity in shear resistance and the presence of foreshocks contribute to a more abrupt mainshock nucleation, contrasting with the smoother, more predictable behavior in $Model\ A$.

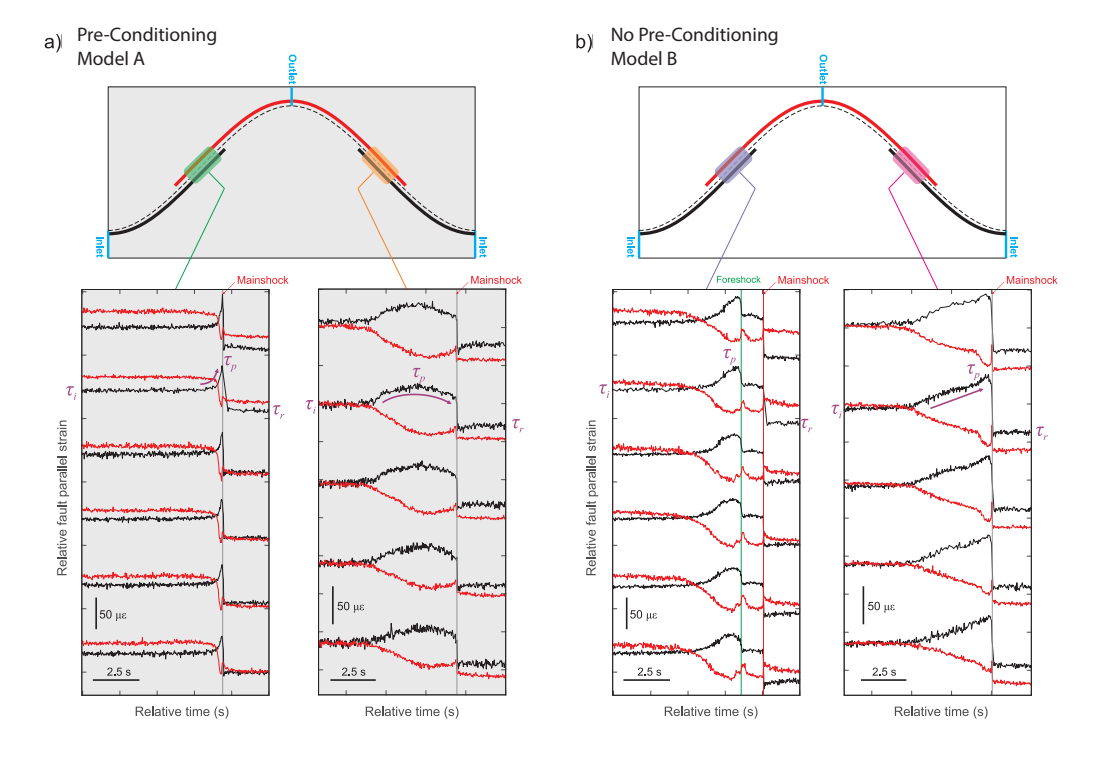


Figure 6: Fault-parallel DSS array measurements at two locations along regions of the fault where data from both the FW (red lines) and HW (black lines) were available. (a) Strain response in the final moments before failure in the pre-conditioned fault (Test 6). (b) Strain response in the final moments before dynamic failure in the not pre-conditioned fault (Test 4).

Furthermore, sustained pore fluid pressure increase during pre-conditioning significantly influences fault strength and heterogeneity. Elevated pore-pressure reduces the effective normal stress on the fault, facilitating rupture without additional shear stress changes. This promotes a more uniform stress distribution and smoother slip propagation across larger fault segments, consistent with the rupture dynamics reflected in *Model A*. Such fluid-driven weakening enhances the potential for larger, more coherent rupture events, playing a crucial role in fault stability and earthquake nucleation.

Conversely, rapid fluid pressurization in not pre-conditioned faults prevents smoothing of shear resistance heterogeneities, leading to the formation of barriers that can cause foreshocks. These localized instabilities complicate rupture nucleation, resulting in an abrupt mainshock with less predictability – more characteristic of *Model B*. While foreshocks at the scale of the nucleation zone may offer insights into mainshock timing (Mignan, 2014; Selvadurai and Glaser, 2015), they also introduce barriers that can precipitate sudden, abrupt ruptures (Selvadurai et al., 2023).

Despite the compelling nature of these results, some irregularities remain. Notably, the strain response in the FW (red lines in Fig. 6) appears mirrored on the HW; however, during dynamic rupture, fault-parallel strain redistributes locally in ways not captured by current models. We attribute this to the finite geometry of the saw-cut, triaxially confined samples contributing to boundary condition effects rarely discussed in the literature (Michail et al., 2025). These factors are not yet fully integrated into our interpretation, but ongoing numerical work to simulate shear slip kinematics along the fault is underway following Dublanchet et al. (2024). We note that the strain response in Fig. 6 is assumed to be proportional to shear stresses but more rigorous models are necessary to perform a more quantitative analysis.

4.3.2. Quantification of the Asymmetrical Fault Response

In the previous sections, we showed that fluid pre-conditioning appears to promote a more asymmetric deformational response along the fault (see discussion of Model A in Section 4.3.1) compared to the tests performed without it (see discussion of Model B in Section 4.3.1). To quantify the symmetry of such response between the left and right sides of the fault, we determined the Pearson correlation coefficient (Pearson, 1895) between the DSS measurements of the left side of the fault-parallel segment $(P_3 \rightarrow P_4)$ with the ones of the inverted right side of it $(P_5 \rightarrow P_4)$ for each measurement in time retrieved during the six reactivation tests. Figure 7 shows the centered moving average of the Pearson correlation coefficients determined for each test, applied using a two-second window to smooth the correlation signals. The correlation coefficients of the FW are generally close to 1 in all reactivation tests, indicating a high level of symmetry between the two sides of the fault. However, we believe this is due to the prominent extensional peak (Fig. 3) observed near the fiber segment point P_4^{FW} , which saturates the strain measurements and is caused by the borehole deformation during injection. On the other hand, the correlation analysis performed on the fiber segments of the HW shows differences between tests performed without (Figs. 7a, c and d) or with (Figs. 7b, e and f) fluid pre-conditioning. The tests adopting the studied injection protocol display Pearson correlation coefficients that are lower with respect to the ones without it, indicating that a more asymmetric fault deformation response is induced when employing fluid pre-conditioning.

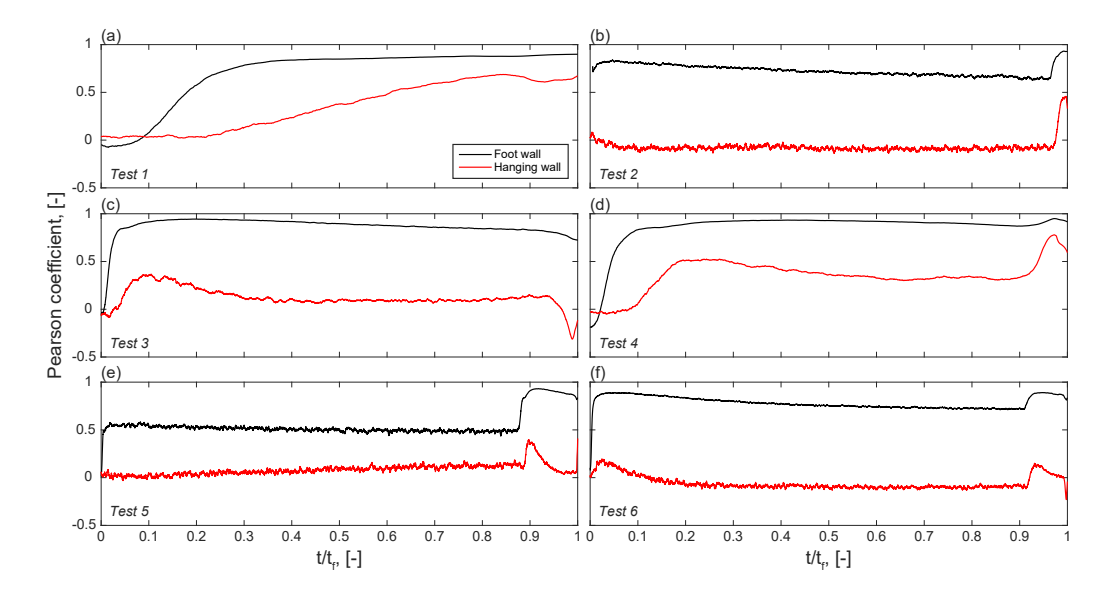


Figure 7: (a)-(f) Centered moving average of the Pearson correlation coefficients determined between the DSS measurements of the right and left sides of the fault-parallel segments in the HW (red) and FW (black) for the $Test\ 1$ - $Test\ 6$, respectively, as a function of the normalized time to failure.

5. Conclusions

We investigated the effect of fluid pre-conditioning on the deformational response of a critically stressed, laboratory fault by performing injection reactivation tests on a saw-cut sample of Rotondo granite confined at 20 MPa. Six reactivation tests and their associated stick-slip events are analyzed: three tests with fluid pre-conditioning and three without. DSS was used to track the total deformation and 16 PZTs are employed, both actively and passively, to track P-wave velocity variations associated with fluid diffusion along the fault and to detect fluid-induced stick-slip events. DSS measurements show the development of a heterogeneous deformation response of the sample in response to the injection of pressurized water.

By relying on the seminal work of Ohnaka (1992) combined with the laboratory measurements presented here, we propose two conceptual models explaining the differences in the fault deformational response observed during the six tests. In the pre-conditioned tests, fluid injection promotes strain localization along the fault through channelized fluid flow, as confirmed by the ultrasonic measurements. The fault-parallel DSS data reveal a predominantly aseismic nucleation phase, characterized by a gradual strain accumulation on one side of the fault and a rapid rupture initiation on the other. The sustained pore pressure increase typical of the pre-conditioning phase reduces the effective normal stress along the fault, smooths stress heterogeneities, and enables larger, more coherent rupture propagation.

Conversely, in the non pre-conditioned tests, the observed rupture nucleation is more heterogeneous and complex, involving localized instabilities and foreshocks that can cause abrupt stress drops and, consequently, accelerate the nucleation growth. Rapid fluid pressurization preserves shear resistance heterogeneities, creating barriers that complicate the rupture development. These effects result in less predictable, more abrupt mainshocks with a complex nucleation behavior.

Further research will include testing the effect of fluid pre-conditioning on the deformational response of rougher fault surfaces. We acknowledge that natural faults have greater complexity and we believe that, even though we have performed this investigation on a relatively smooth interface, our findings are promising and may provide insights that could help design injection protocols that aim to reduce the risk of induced seismicity in geoenergy projects.

Acknowledgments and Funding

The authors would like to acknowledge Dr. Alba Zappone for providing the tested rock sample and Dr. Mehdi Nikkhoo for fruitful discussions on topics related to the investigation. We thank Hao Chen, Markus Rast and Sofia Michail for the support provided during the experimental operations and Thomas Mörgeli for the technical support. Funding for P. Bianchi was provided from the Swiss National Science Foundation (SNSF) (No. 200021-192017). Partial funding for P. A. Selvadurai was provided from the European Research Council (ERC) project FEAR (grant 856559) under the European Community's Horizon 2020 Framework Programme Funds. A. F. Salazar Vásquez would like to thank the Innosuisse FLAGSHIP project "AEGIS-CH: Advanced geothermal systems to improve the resilience of the energy supply of Switzerland" (No. 2150009483) for the financial support. The authors would like to acknowledge the Swiss Seismological Service and

the Swiss National Science Foundation with the project R'Equip206021-170766 – "Physical constraints on natural and induced earthquakes using innovative lab scale experiments: The LabQuake Machine".

Data Availability

The data sets related to the investigations presented here may be made open-source by private consultation with the authors.

Supplementary Material

Supplementary material is available and attached to this manuscript as a separate document.

Competing Interests

The authors have no competing interests.

References

- Akaike, H., 1974. A new look at the statistical model identification. IEEE Transactions on Automatic Control 19, 716–723. doi:10.1109/TAC.1974.1100705.
- Almakari, M., Dublanchet, P., Chauris, H., Pellet, F., 2019. Effect of the Injection Scenario on the Rate and Magnitude Content of Injection-Induced Seismicity: Case of a Heterogeneous Fault. Journal of Geophysical Research: Solid Earth 124, 8426–8448. doi:https://doi.org/10.1029/2019JB017898.
- Bense, V.F., Gleeson, T., Loveless, S., Bour, O., Scibek, J., 2013. Fault zone hydrogeology. Earth-Science Reviews 127, 171-192. doi:https://doi.org/10.1016/j.earscirev.2013.09.008.
- Bianchi, P., Selvadurai, P.A., Vasquez, A.S., Dal Zilio, L., Gerya, T., Madonna, C., Wiemer, S., 2022. A study of progressive failure in porous rocks using numerical and experimental modeling. 56th U.S. Rock Mechanics/Geomechanics Symposium doi:10.56952/ARMA-2022-0621.
- Bianchi, P., Selvadurai, P.A., Zilio, L.D., Vásquez, A.S., Madonna, C., Gerya, T., Wiemer, S., 2024. Pre-Failure Strain Localization in Siliclastic Rocks: A Comparative Study of Laboratory and Numerical Approaches. Rock Mechanics and Rock Engineering doi:10.1007/s00603-024-04025-y.
- Cappa, F., Guglielmi, Y., Nussbaum, C., Birkholzer, J., 2018. On the Relationship Between Fault Permeability Increases, Induced Stress Perturbation, and the Growth of Aseismic Slip During Fluid Injection. Geophysical Research Letters 45, 11,012–11,020. doi:https://doi.org/10.1029/2018GL080233.
- Cappa, F., Scuderi, M.M., Collettini, C., Guglielmi, Y., Avouac, J.P., 2019. Stabilization of fault slip by fluid injection in the laboratory and in situ. Science Advances 5, eaau4065. doi:10.1126/sciadv.aau4065.
- Cattania, C., Segall, P., 2021. Precursory slow slip and foreshocks on rough faults. Journal of Geophysical Research: Solid Earth 126, e2020JB020430. doi:https://doi.org/10.1029/2020JB020430.

- Cebry, S.B.L., McLaskey, G.C., 2021. Seismic swarms produced by rapid fluid injection into a low permeability laboratory fault. Earth and Planetary Science Letters 557, 116726. doi:https://doi.org/10.1016/j.epsl. 2020.116726.
- David, C., Nejati, M., Geremia, D., 2020. On petrophysical and geomechanical properties of Bedretto Granite. Report. ETH Zurich. Zurich. doi:10.3929/ethz-b-000428267.
- Deichmann, N., Giardini, D., 2009. Earthquakes Induced by the Stimulation of an Enhanced Geothermal System below Basel (Switzerland). Seismological Research Letters 80, 784–798. doi:10.1785/gssrl.80.5.784.
- Dieterich, J.H., 1979. Modeling of rock friction: 1. experimental results and constitutive equations. Journal of Geophysical Research: Solid Earth 84, 2161–2168. doi:https://doi.org/10.1029/JB084iB05p02161.
- Dieterich, J.H., 1992. Earthquake nucleation on faults with rate-and state-dependent strength. Tectonophysics 211, 115–134. doi:https://doi.org/10.1016/0040-1951(92)90055-B.
- Dieterich, J.H., Kilgore, B.D., 1994. Direct observation of frictional contacts: New insights for state-dependent properties. Pure and Applied Geophysics 143, 283–302. doi:10.1007/BF00874332.
- Dublanchet, P., Passelègue, F.X., Chauris, H., Gesret, A., Twardzik, C., Nöel, C., 2024. Kinematic inversion of aseismic fault slip during the nucleation of laboratory earthquakes. Journal of Geophysical Research: Solid Earth 129, e2024JB028733. doi:https://doi.org/10.1029/2024JB028733.
- Fang, Z., Wu, W., 2022. Laboratory friction-permeability response of rock fractures: a review and new insights. Geomechanics and Geophysics for Geo-Energy and Geo-Resources 8, 15. doi:10.1007/s40948-021-00316-8.
- French, M.E., Zhu, W., Banker, J., 2016. Fault slip controlled by stress path and fluid pressurization rate. Geophysical Research Letters 43, 4330–4339. doi:https://doi.org/10.1002/2016GL068893.

- Galis, M., Ampuero, J.P., Mai, P.M., Cappa, F., 2017. Induced seismicity provides insight into why earthquake ruptures stop. Science Advances 3, eaap7528. doi:10.1126/sciadv.aap7528.
- Garagash, D.I., Germanovich, L.N., 2012. Nucleation and arrest of dynamic slip on a pressurized fault. Journal of Geophysical Research: Solid Earth 117. doi:https://doi.org/10.1029/2012JB009209.
- Goebel, T.H.W., Schuster, V., Kwiatek, G., Pandey, K., Dresen, G., 2024. A laboratory perspective on accelerating preparatory processes before earth-quakes and implications for foreshock detectability. Nature Communications 15, 5588. doi:10.1038/s41467-024-49959-7.
- Grigoli, F., Cesca, S., Rinaldi, A.P., Manconi, A., López-Comino, J.A., Clinton, J.F., Westaway, R., Cauzzi, C., Dahm, T., Wiemer, S., 2018. The November 2017 <i>M</i>_w 5.5 Pohang earthquake: A possible case of induced seismicity in South Korea. Science 360, 1003–1006. doi:10.1126/science.aat2010.
- Guglielmi, Y., Cappa, F., Avouac, J.P., Henry, P., Elsworth, D., 2015. Seismicity triggered by fluid injection—induced aseismic slip. Science 348, 1224—1226. doi:10.1126/science.aab0476.
- Hubbert, M., Rubey, W., 1959. Role of Fluid Pressure in Mechanics of Overthrust Faulting: I. Mechanics of Fluid-Filled Porous Solids and its Application to Overthrust Faulting. GSA Bulletin 70, 115–166. doi:10. 1130/0016-7606(1959)70[115:R0FPIM]2.0.C0;2.
- Huo, J., Selvadurai, A.P.S., Meguid, M., 2024. Permeability Evolution in a Fracture in Granite During Isotropic Compression. Rock Mechanics and Rock Engineering doi:10.1007/s00603-024-03875-w.
- Ida, Y., 1972. Cohesive force across the tip of a longitudinal-shear crack and griffith's specific surface energy. Journal of Geophysical Research (1896-1977) 77, 3796–3805. doi:https://doi.org/10.1029/JB077i020p03796.
- Ji, Y., Wang, L., Hofmann, H., Kwiatek, G., Dresen, G., 2022. High-Rate Fluid Injection Reduces the Nucleation Length of Laboratory Earthquakes on Critically Stressed Faults in Granite. Geophysical Research Letters 49, e2022GL100418. doi:https://doi.org/10.1029/2022GL100418.

- Lui, S.K.Y., Huang, Y., Young, R.P., 2021. The role of fluid pressure-induced aseismic slip in earthquake cycle modulation. Journal of Geophysical Research: Solid Earth 126, e2020JB021196. doi:https://doi.org/10.1029/2020JB021196.
- Ma, X., Hertrich, M., Amann, F., Bröker, K., Gholizadeh Doonechaly, N., Gischig, V., Hochreutener, R., Kästli, P., Krietsch, H., Marti, M., Nägeli, B., Nejati, M., Obermann, A., Plenkers, K., Rinaldi, A.P., Shakas, A., Villiger, L., Wenning, Q., Zappone, A., Bethmann, F., Castilla, R., Seberto, F., Meier, P., Driesner, T., Loew, S., Maurer, H., Saar, M.O., Wiemer, S., Giardini, D., 2022. Multi-disciplinary characterizations of the BedrettoLab a new underground geoscience research facility. Solid Earth 13, 301–322. doi:10.5194/se-13-301-2022.
- McLaskey, G.C., 2019. Earthquake initiation from laboratory observations and implications for foreshocks. Journal of Geophysical Research: Solid Earth 124, 12882–12904. doi:https://doi.org/10.1029/2019JB018363.
- Michail, S., Selvadurai, P.A., Rast, M., Salazar Vásquez, A.F., Bianchi, P., Madonna, C., Wiemer, S., 2025. Strain heterogeneities in laboratory faults driven by roughness and wear. Earth and Planetary Science Letters 657, 119247. doi:https://doi.org/10.1016/j.epsl.2025.119247.
- Mignan, A., 2014. The debate on the prognostic value of earthquake foreshocks: A meta-analysis. Scientific Reports 4, 4099. doi:10.1038/srep04099.
- Mignan, A., Landtwing, D., Kästli, P., Mena, B., Wiemer, S., 2015. Induced seismicity risk analysis of the 2006 Basel, Switzerland, Enhanced Geothermal System project: Influence of uncertainties on risk mitigation. Geothermics 53, 133–146. doi:https://doi.org/10.1016/j.geothermics.2014.05.007.
- Moein, M.J.A., Langenbruch, C., Schultz, R., Grigoli, F., Ellsworth, W.L., Wang, R., Rinaldi, A.P., Shapiro, S., 2023. The physical mechanisms of induced earthquakes. Nature Reviews Earth & Environment 4, 847–863. doi:10.1038/s43017-023-00497-8.
- Noda, H., Nakatani, M., Hori, T., 2013. Large nucleation before large earthquakes is sometimes skipped due to cascade-up—implications from

- a rate and state simulation of faults with hierarchical asperities. Journal of Geophysical Research: Solid Earth 118, 2924–2952. doi:https://doi.org/10.1002/jgrb.50211.
- Noël, C., Passelègue, F.X., Giorgetti, C., Violay, M., 2019. Fault Reactivation During Fluid Pressure Oscillations: Transition From Stable to Unstable Slip. Journal of Geophysical Research: Solid Earth 124, 10940–10953. doi:https://doi.org/10.1029/2019JB018517.
- Ohnaka, M., 1992. Earthquake source nucleation: A physical model for short-term precursors. Tectonophysics 211, 149–178. doi:https://doi.org/10.1016/0040-1951(92)90057-D.
- Ohnaka, M., 2003. A constitutive scaling law and a unified comprehension for frictional slip failure, shear fracture of intact rock, and earthquake rupture. Journal of Geophysical Research: Solid Earth 108. doi:https://doi.org/10.1029/2000JB000123.
- Ohnaka, M., Shen, L.f., 1999. Scaling of the shear rupture process from nucleation to dynamic propagation: Implications of geometric irregularity of the rupturing surfaces. Journal of Geophysical Research: Solid Earth 104, 817–844. doi:https://doi.org/10.1029/1998JB900007.
- Passelègue, F.X., Brantut, N., Mitchell, T.M., 2018. Fault Reactivation by Fluid Injection: Controls From Stress State and Injection Rate. Geophysical Research Letters 45, 12,837–12,846. doi:https://doi.org/10.1029/2018GL080470.
- Pearson, K., 1895. Note on regression and inheritance in the case of two parents. Proceedings of the Royal Society of London Series I 58, 240–242.
- Proctor, B., Lockner, D.A., Kilgore, B.D., Mitchell, T.M., Beeler, N.M., 2020. Direct Evidence for Fluid Pressure, Dilatancy, and Compaction Affecting Slip in Isolated Faults. Geophysical Research Letters 47, e2019GL086767. doi:https://doi.org/10.1029/2019GL086767.
- Pyrak-Nolte, L.J., Nolte, D.D., 2016. Approaching a universal scaling relationship between fracture stiffness and fluid flow. Nature Communications 7, 10663. doi:10.1038/ncomms10663.

- Rast, M., Galli, A., Ruh, J.B., Guillong, M., Madonna, C., 2022. Geology along the Bedretto tunnel: kinematic and geochronological constraints on the evolution of the Gotthard Massif (Central Alps). Swiss Journal of Geosciences 115. URL: https://doi.org/10.1186/s00015-022-00409-w, doi:10.1186/s00015-022-00409-w.
- Rast, M., Madonna, C., Selvadurai, P.A., Wenning, Q.C., Ruh, J.B., 2024. Importance of Water-Clay Interactions for Fault Slip in Clay-Rich Rocks. Journal of Geophysical Research: Solid Earth 129, e2023JB028235. doi:https://doi.org/10.1029/2023JB028235.
- Rezaei Niya, S., Selvadurai, A., 2019. Correlation of joint roughness coefficient and permeability of a fracture. International Journal of Rock Mechanics and Mining Sciences 113, 150–162. doi:https://doi.org/10.1016/j.ijrmms.2018.12.008.
- Rubin, A.M., Ampuero, J.P., 2005. Earthquake nucleation on (aging) rate and state faults. Journal of Geophysical Research: Solid Earth 110. doi:https://doi.org/10.1029/2005JB003686.
- Salazar Vásquez, A., Selvadurai, P.A., Bianchi, P., Madonna, C., Germanovich, L.N., Puzrin, A.M., Wiemer, S., Giardini, D., Rabaiotti, C., 2024. Aseismic strain localization prior to failure and associated seismicity in crystalline rock. Scientific Reports.
- Salazar Vásquez, A.F., Rabaiotti, C., Germanovich, L.N., Puzrin, A.M., 2022. Distributed Fiber Optics Measurements of Rock Deformation and Failure in Triaxial Tests. Journal of Geophysical Research: Solid Earth 127, e2022JB023997. doi:https://doi.org/10.1029/2022JB023997.
- Scheck-Wenderoth, M., Schmeisser, D., Mutti, M., Kolditz, O., Huenges, E., Schultz, H.M., Liebscher, A., Bock, M., 2013. Geoenergy: new concepts for utilization of geo-reservoirs as potential energy sources. Environmental Earth Sciences 70, 3427–3431. doi:10.1007/s12665-013-2877-y.
- Scuderi, M.M., Collettini, C., 2018. Fluid Injection and the Mechanics of Frictional Stability of Shale-Bearing Faults. Journal of Geophysical Research: Solid Earth 123, 8364–8384. doi:https://doi.org/10.1029/2018JB016084.

- Segall, P., Rice, J.R., 1995. Dilatancy, compaction, and slip instability of a fluid-infiltrated fault. Journal of Geophysical Research: Solid Earth 100, 22155–22171. doi:https://doi.org/10.1029/95JB02403.
- Selvadurai, P., Galvez, P., Mai, P., Glaser, S., 2023. Modeling frictional precursory phenomena using a wear-based rate- and state-dependent friction model in the laboratory. Tectonophysics 847, 229689. doi:https://doi.org/10.1016/j.tecto.2022.229689.
- Selvadurai, P.A., Glaser, S., 2017. Asperity generation and its relationship to seismicity on a planar fault: a laboratory simulation. Geophysical Journal International 208, 1009–1025. doi:10.1093/gji/ggw439.
- Selvadurai, P.A., Glaser, S.D., 2015. Laboratory-developed contact models controlling instability on frictional faults. Journal of Geophysical Research: Solid Earth 120, 4208–4236. doi:https://doi.org/10.1002/2014JB011690.
- Selvadurai, P.A., Selvadurai, A.P.S., 2025. On the Influence of a Dilatant Asperity Patch on the Seismic Moment. Journal of Elasticity 157, 44. doi:10.1007/s10659-025-10135-7.
- Selvadurai, P.A., Wu, R., Bianchi, P., Niu, Z., Michail, S., Madonna, C., Wiemer, S., 2022. A Methodology for Reconstructing Source Properties of a Conical Piezoelectric Actuator Using Array-Based Methods. Journal of Nondestructive Evaluation 41. doi:10.1007/s10921-022-00853-6.
- Terzaghi, K., 1936. The shearing resistance of saturated soils. Proc. 1st Int. Conf. Soil Mech. 1, 54–56.
- Trutnevyte, E., Wiemer, S., 2017. Tailor-made risk governance for induced seismicity of geothermal energy projects: An application to Switzerland. Geothermics 65, 295–312. doi:https://doi.org/10.1016/j.geothermics.2016.10.006.
- Villiger, L., Gischig, V.S., Doetsch, J., Krietsch, H., Dutler, N.O., Jalali, M., Valley, B., Selvadurai, P.A., Mignan, A., Plenkers, K., Giardini, D., Amann, F., Wiemer, S., 2020. Influence of reservoir geology on seismic response during decameter-scale hydraulic stimulations in crystalline rock. Solid Earth 11, 627–655. doi:10.5194/se-11-627-2020.

- Vogler, D., Settgast, R.R., Annavarapu, C., Madonna, C., Bayer, P., Amann, F., 2018. Experiments and Simulations of Fully Hydro-Mechanically Coupled Response of Rough Fractures Exposed to High-Pressure Fluid Injection. Journal of Geophysical Research: Solid Earth 123, 1186–1200. doi:https://doi.org/10.1002/2017JB015057.
- Wang, L., Kwiatek, G., Renard, F., Guérin-Marthe, S., Rybacki, E., Bohnhoff, M., Naumann, M., Dresen, G., 2024. Fault roughness controls injection-induced seismicity. Proceedings of the National Academy of Sciences 121, e2310039121. doi:10.1073/pnas.2310039121.
- Wang, L., Kwiatek, G., Rybacki, E., Bonnelye, A., Bohnhoff, M., Dresen, G., 2020. Laboratory Study on Fluid-Induced Fault Slip Behavior: The Role of Fluid Pressurization Rate. Geophysical Research Letters 47, e2019GL086627. doi:https://doi.org/10.1029/2019GL086627.
- Wenning, Q.C., Madonna, C., Kurotori, T., Petrini, C., Hwang, J., Zappone, A., Wiemer, S., Giardini, D., Pini, R., 2021. Chemo-Mechanical Coupling in Fractured Shale With Water and Hydrocarbon Flow. Geophysical Research Letters 48, e2020GL091357. doi:https://doi.org/10.1029/2020GL091357.
- Wu, B., Barbot, S., 2025. Evolution of the real area of contact during laboratory earthquakes. Proceedings of the National Academy of Sciences 122, e2410496122. doi:10.1073/pnas.2410496122.
- Wynants-Morel, N., Cappa, F., De Barros, L., Ampuero, J.P., 2020. Stress Perturbation From Aseismic Slip Drives the Seismic Front During Fluid Injection in a Permeable Fault. Journal of Geophysical Research: Solid Earth 125, e2019JB019179. doi:https://doi.org/10.1029/2019JB019179.
- Ye, Z., Ghassemi, A., 2018. Injection-Induced Shear Slip and Permeability Enhancement in Granite Fractures. Journal of Geophysical Research: Solid Earth 123, 9009–9032. doi:https://doi.org/10.1029/2018JB016045.
- Zimmerman, R.W., Chen, D.W., Cook, N.G., 1992. The effect of contact area on the permeability of fractures. Journal of Hydrology 139, 79–96. doi:https://doi.org/10.1016/0022-1694(92)90196-3.
- Zimmermann, G., Reinicke, A., 2010. Hydraulic stimulation of a deep sandstone reservoir to develop an Enhanced Geothermal System: Laboratory

and field experiments. Geothermics 39, 70-77. doi:https://doi.org/10.1016/j.geothermics.2009.12.003.

Supplementary Material for "The Effects of Fluid Pre-Conditioning on the Deformational Response of a Laboratory Fault"

P.Bianchi*, P. A. Selvadurai, A. Salazar Vásquez, C. Madonna, S. Wiemer

*Corresponding author: patrick.bianchi@sed.ethz.ch;

- 16th October 2025 -

1 Processing of Macroscopical Mechanical Measurements

During all tests presented in the main manuscript, the radial stress σ_3 is applied using a temperature-resistant hydraulic oil through the jacket and the axial stress σ_1 is imposed with a servo-controlled piston. Both parameters are measured at 1 Hz. To convert these into a framework more conventional to saw-cut experiments, we determine the normal σ_N and shear τ stresses as:

$$\sigma_N = \frac{\sigma_1 + \sigma_3}{2} + \frac{\sigma_1 - \sigma_3}{2} \cdot \cos(2\theta) \tag{1}$$

and

$$\tau = \frac{\sigma_1 - \sigma_3}{2} \cdot \sin(2\theta),\tag{2}$$

where θ is the angle between the fault normal and the axial axis of the sample. In our study, $\theta = 90^{\circ}$ - $\varphi = 55^{\circ}$ (Fig. 1 of the main manuscript). The slip ΔS along the fault caused by the observed stick-slip events is estimated by:

$$\Delta S = \frac{\Delta L_{LVDT}}{\cos(\varphi)},\tag{3}$$

with ΔL_{LVDT} being the axial shortening measured by the LVDT. The slip is necessary to estimate the scalar seismic moment M_0 associated to each stick-slip event as $M_0 = A \cdot \Delta S \cdot G$, where A is the area of the ellipsoidal fracture of the sample and G = 20.1 GPa is the shear modulus (Salazar Vásquez et al., 2024).

2 Dry Failure Envelope Tests

We determined the Mohr-Coulomb failure envelope (Scholz, 2019) of the Rotondo granite fault in dry conditions by inducing consecutive stick-slip events due to an increase of the fault shear stress above its strength at confining pressures $\sigma_3 = 80$, 40, 20 and 10 MPa. Figure S1a shows the protocol followed during these tests. While maintaining the confining pressure constant, we increase the shear stress on the fault with a constant displacement velocity of the piston of 1 μ m/s until we observe a stick-slip event.

We retrieve the shear stress τ and normal stress σ_N before (i.e., peak) and after (i.e., residual) the stress drop of each stick-slip event and display them in a scatter plot (Fig. S1b). By fitting a line between the peak and residual points, we construct the dry failure envelopes $\tau = 0.55 \cdot \sigma_N + 6.93$ MPa and $\tau = 0.50 \cdot \sigma_N + 6.34$ MPa (Eq. 1 of the main manuscript), respectively. We consider the stick-slip events observed at peaks 1, 2 and 3 (highlighted in Fig. S1b with red arrows) to be associated with partial slip events that do not rupture the entire fault but only regions of it (Selvadurai et al., 2017). These are excluded from the determination of the failure envelope. Our results are in the same range of values found in the literature for granitic lithologies (Paterson and Wong, 2005). Additional parameters, such as the apparent friction τ/σ_N or the scalar seismic moment M_0 associated to each stick-slip event, are determined and provided in the Supplementary Material 9.

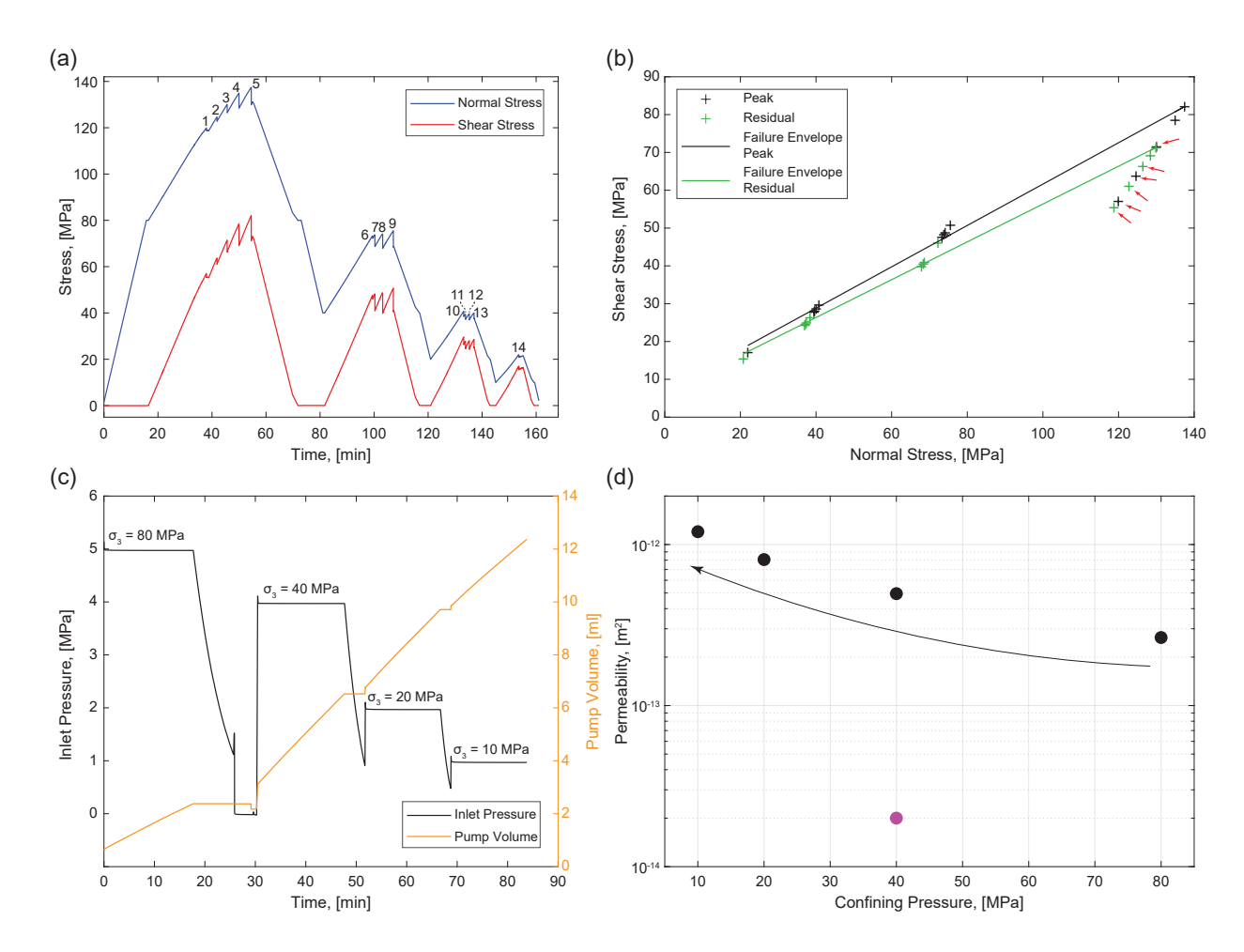


Fig. S1 (a) Normal (blue) and shear (red) stresses imposed during the dry failure envelope tests as a function of time. The number above the peaks of normal stress indicate the stick-slips observed. (b) Dry failure envelope for the peak (black) and residual (green) cases. The peaks and residual points are marked with crosses and are retrieved in (a). The red arrows indicate the peaks discarded from the fitting of the envelopes. (c) Inlet pressure (black) and injected volume (orange) imposed during the hydrostatic permeability tests as a function of time. (d) Permeability values for the hydrostatic cases (black dots) and under both shear and normal stress conditions (violet dot) as a function of the confining pressure applied. The arrow indicates the order of the tests performed in the hydrostatic case.

3 Permeability Tests

We performed permeability tests in hydrostatic and drained (i.e., outlet open to atmospheric pressure) conditions at confining pressures $\sigma_3 = 80$, 40, 20 and 10 MPa. An additional permeability test, also in drained conditions, is carried out at a confining pressure of 40 MPa, with critical shear stress conditions (80% of the fault strength, $\sigma_1 = 125.7$ MPa) imposed on the fracture. By combining the cubic law (Witherspoon et al., 1980; Zimmerman and Bodvarsson, 1996), which links the permeability k to the equivalent hydraulic aperture a_h , with Darcy's law, we determine the permeability of the fracture as (Ye and Ghassemi, 2018):

$$k = \frac{a_h^2}{12} = \frac{1}{12} \cdot \left(-\frac{12\mu LQ}{W\Delta P} \right)^{2/3},\tag{4}$$

where μ is the fluid viscosity (10⁻³ Pa·s for water at 20 °C), ΔP (units [Pa]) is the pressure gradient between outlet and inlet, Q (units [m³/s]) is the steady flow rate, L=103.9 mm is the distance along the fault surface between the two boreholes and W=73.3 mm is equal to the area of the fault surface divided by L (Ye and Ghassemi, 2018, figure 6b).

Figures S1c and d show the protocols followed during the hydrostatic permeability tests and the determined permeability values (black dots for the hydrostatics cases and violet dot for the permeability at shear and normal stressed conditions) as a function of the confining pressure, respectively. While maintaining hydrostatic stress conditions, we inject water at a constant inlet pressure for ten minutes. This time interval is sufficient for the flow rate Q to stabilize to a constant value. The permeability test at critical stress conditions is carried out in a similar way. The total axial stress is first increased to $\sigma_1 \simeq 125$ MPa and then we hold the piston position while performing the permeability test with the same protocol described for the hydrostatic cases. We retrieve permeability values in the range $10^{-14} - 10^{-12}$ m², which agree with past investigations on granitic lithologies with similar rough fractures (e.g., Ye and Ghassemi, 2018; Huo et al., 2024).

4 Ultrasonic Surveys: Picking Examples

Figure S2 shows picking examples of different source-receiver pairs. The numbers indicated in the figure refer to the PZT numbers provided in Fig. 1c of the main manuscript. In Figs. S2a to f, we provide examples of waveforms recorded from PZT 1-8 of pulses produced by PZT 9-16, respectively.

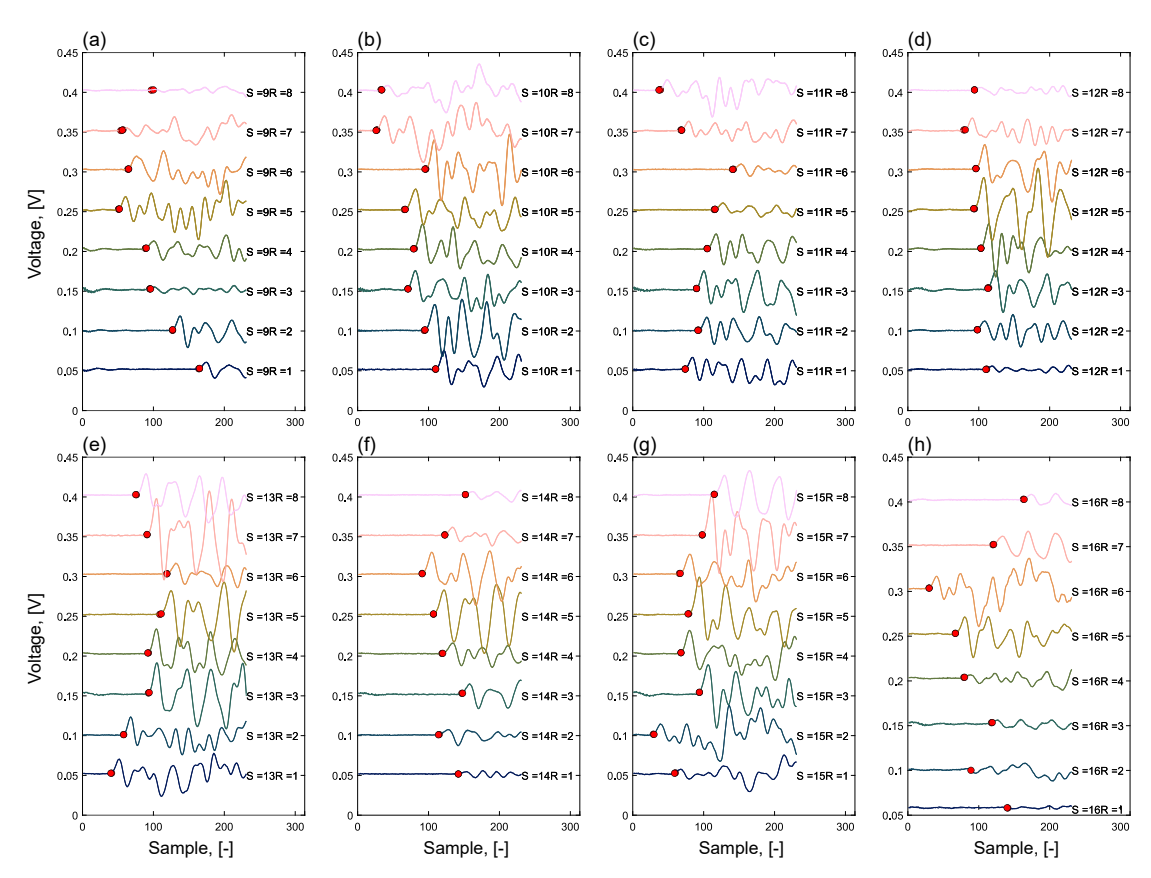


Fig. S2 Examples of the picking (red dots) of the wave arrivals with different source-receiver pairs. The numbers indicated refer to the PZT numbers provided in Fig. 1c of the main manuscript, S is PZT pulsing and R is the PZT recording the waveform.

5 Ultrasonic Surveys: Interpolation Schemes

To test the robustness of the chosen interpolation scheme (i.e., v_4 , see Fig. 4 of the main manuscript), we provide the surface map of the P-wave velocity variations detected during the flooding test (see Section 3.2 of the main manuscript) with three more interpolation schemes of the Matlab function griddata. We show the results of the interpolation schemes natural, nearest and cubic in the Figs. S3, S4 and S5, respectively. These interpolation schemes are all based on a triangulation-based method, which is different from the biharmonic spline interpolation method used by the scheme v_4 . The subfigures a-f refer to the time lapses b-g of Fig.4a of the main manuscript. We note that a channelized fluid flow system can be recognized in Figs. S3, S4 and S5 and it resembles the one presented in Fig. 4 of the main manuscript obtained with the interpolation scheme v_4 .

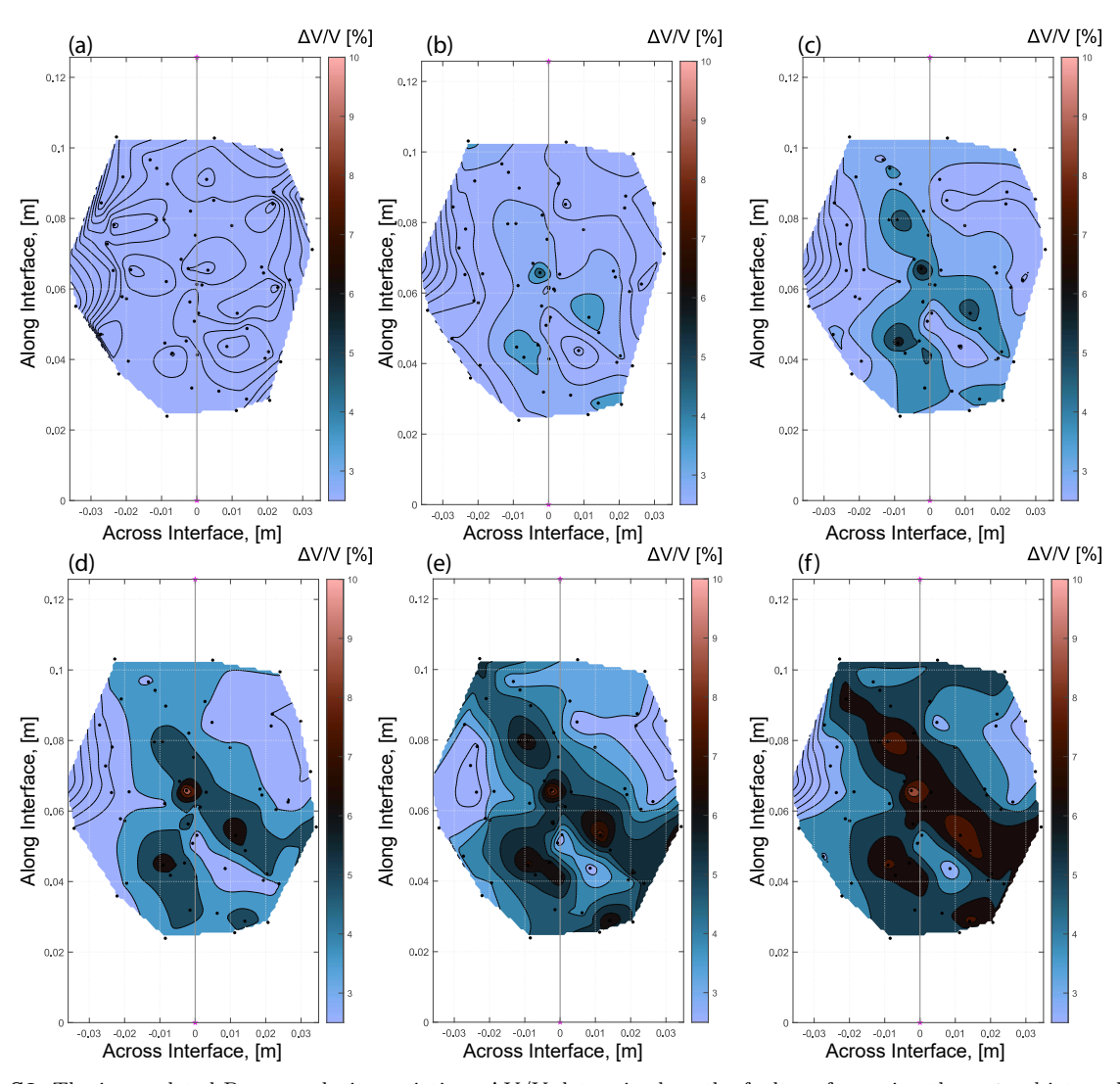


Fig. S3 The interpolated P-wave velocity variations $\Delta V/V$ determined on the fault surface using the *natural* interpolation scheme. (a)-(f) refer to the same time lapses b-g of Fig. 4a of the main manuscript. The black dots show the intersection points of the ray paths between sources and receivers, the pink stars at the bottom and top indicate the inlet and outlet locations, respectively, and the black curves are velocity isolines. The colorbars are normalized with respect to the initial velocity distribution V on the fault surface.

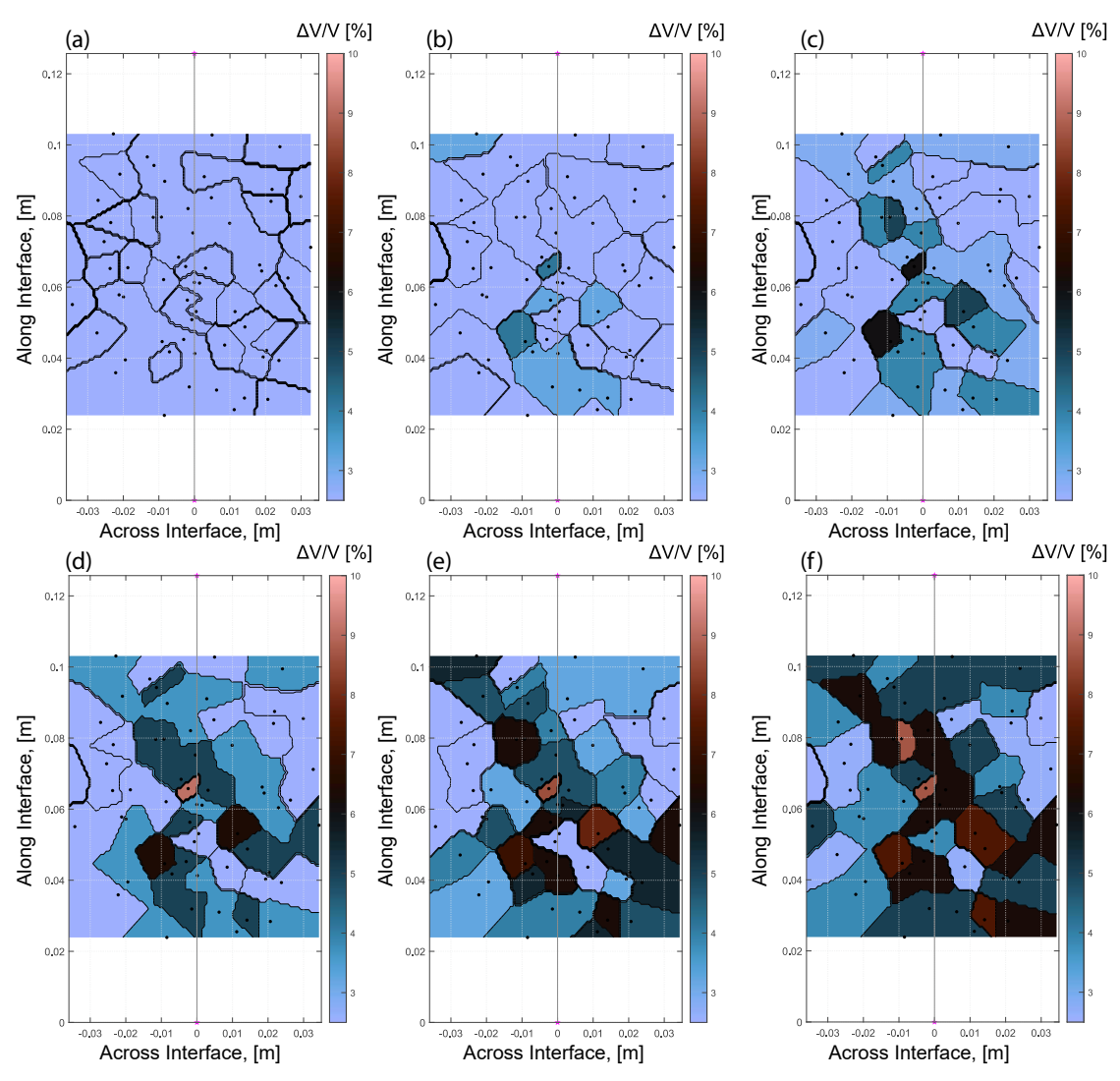


Fig. S4 The interpolated P-wave velocity variations $\Delta V/V$ determined on the fault surface using the *nearest* interpolation scheme. (a)-(f) refer to the same time lapses b-g of Fig. 4a of the main manuscript. The black dots show the intersection points of the ray paths between sources and receivers, the pink stars at the bottom and top indicate the inlet and outlet locations, respectively, and the black curves are velocity isolines. The colorbars are normalized with respect to the initial velocity distribution V on the fault surface.

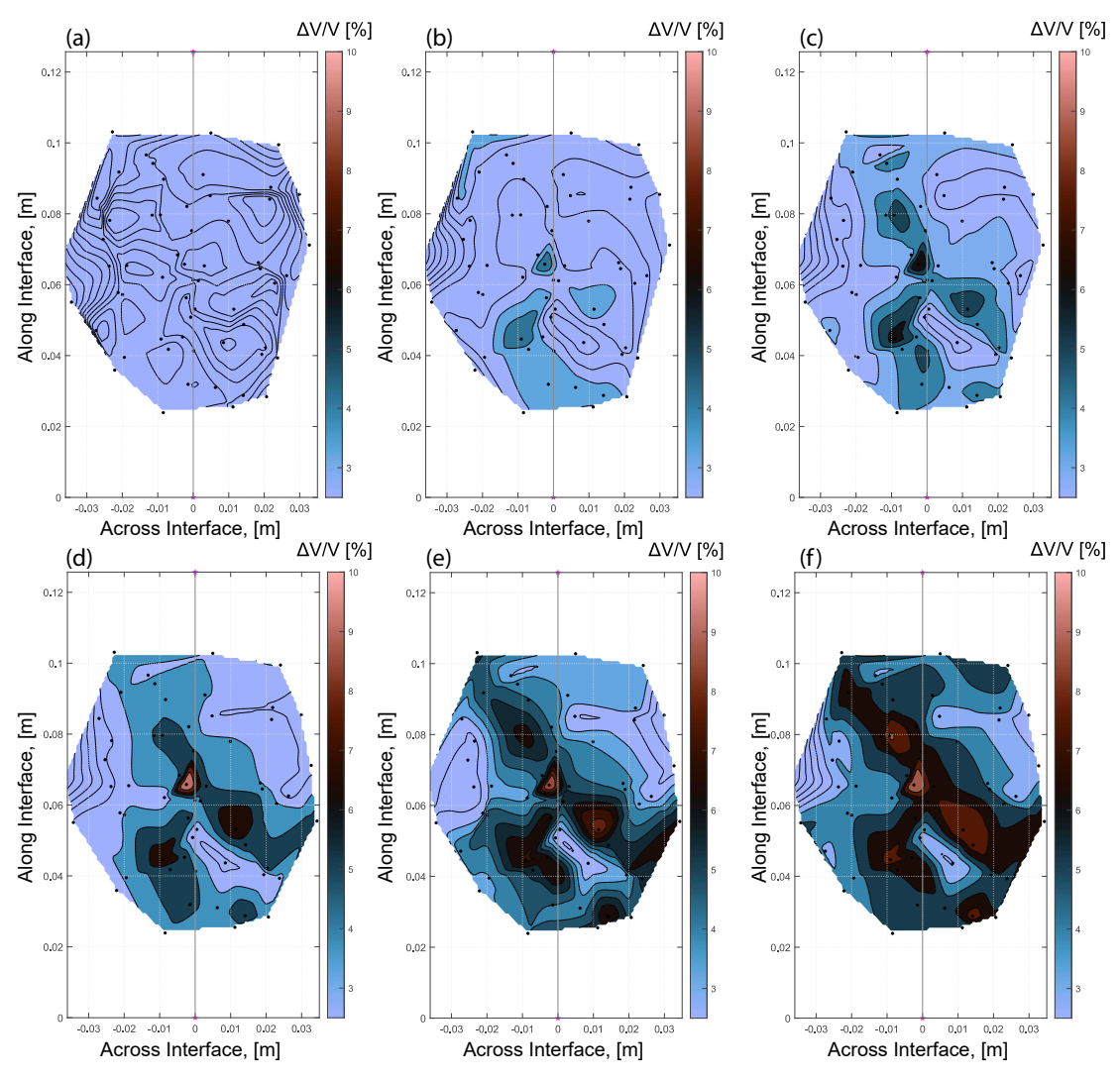


Fig. S5 The interpolated P-wave velocity variations $\Delta V/V$ determined on the fault surface using the *cubic* interpolation scheme. (a)-(f) refer to the same time lapses b-g of Fig. 4a of the main manuscript. The black dots show the intersection points of the ray paths between sources and receivers, the pink stars at the bottom and top indicate the inlet and outlet locations, respectively, and the black curves are velocity isolines. The colorbars are normalized with respect to the initial velocity distribution V on the fault surface.

6 Full Experimental Protocol

Figure S6 shows the full experimental protocol containing the six fluid reactivation tests analyzed in the main manuscript.

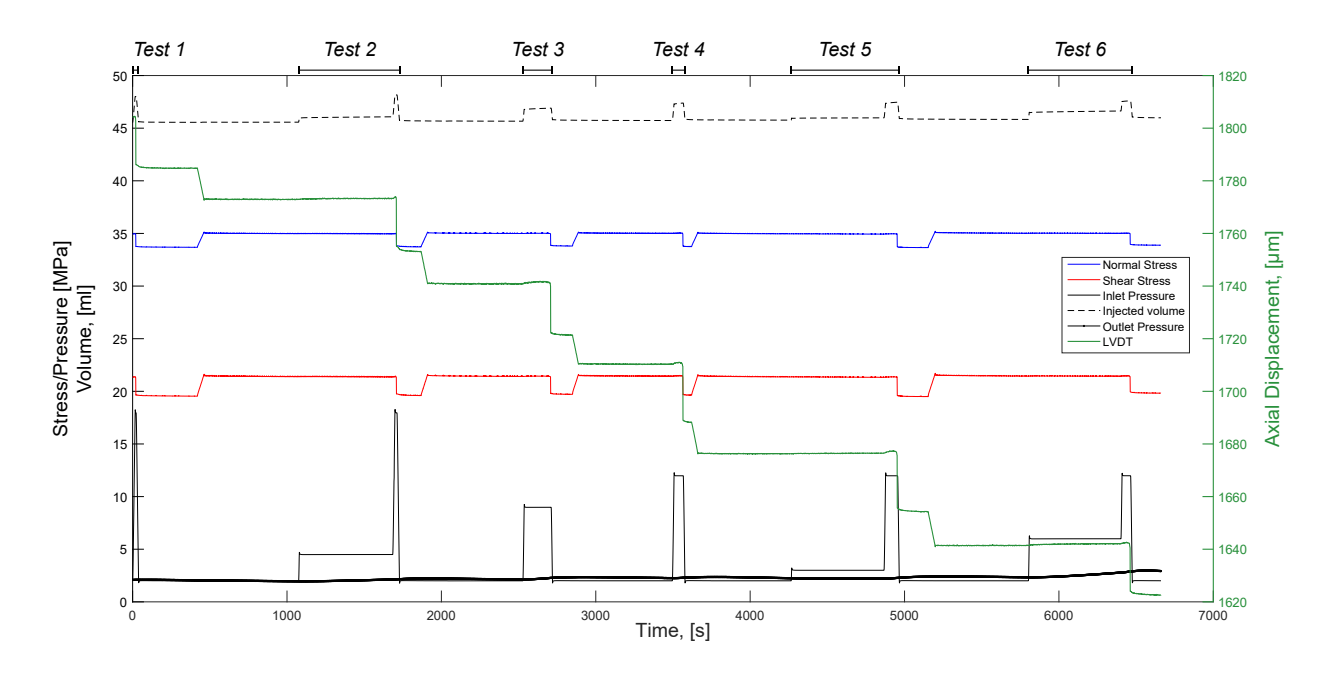


Fig. S6 Full experimental protocol. Normal stress, shear stress, inlet pressure, outlet pressure, injected volume and axial LVDT as a function of time. The intervals of each fluid reactivation test are indicated on top of the figure.

7 Axial Distributed Strain Measurements

Similarly to what was observed with the fault-parallel DSS measurements (see Section 3.1 of the main manuscript), the axial DSS measurements also display heterogeneities along the segments of both sample halves. Figures S7a-f show the axial distributed strain measurements (one of every ten measurements is shown for visualization purposes) of Test 1 to Test 6, respectively. The first and second row display the measurements retrieved in the HW along the segments $P_1^{HW} \to P_2^{HW}$ and $P_6^{HW} \to P_7^{HW}$, whereas the third and fourth rows, respectively, show the same but for the FW. We note that the orientation of the segments in Fig. S7 reflects the actual orientation of the fibers on the sample. The colorbar corresponds to the ones provided in Fig. 2 of the main manuscript, with the light blue lines indicating the measurements retrieved after the stick-slip events.

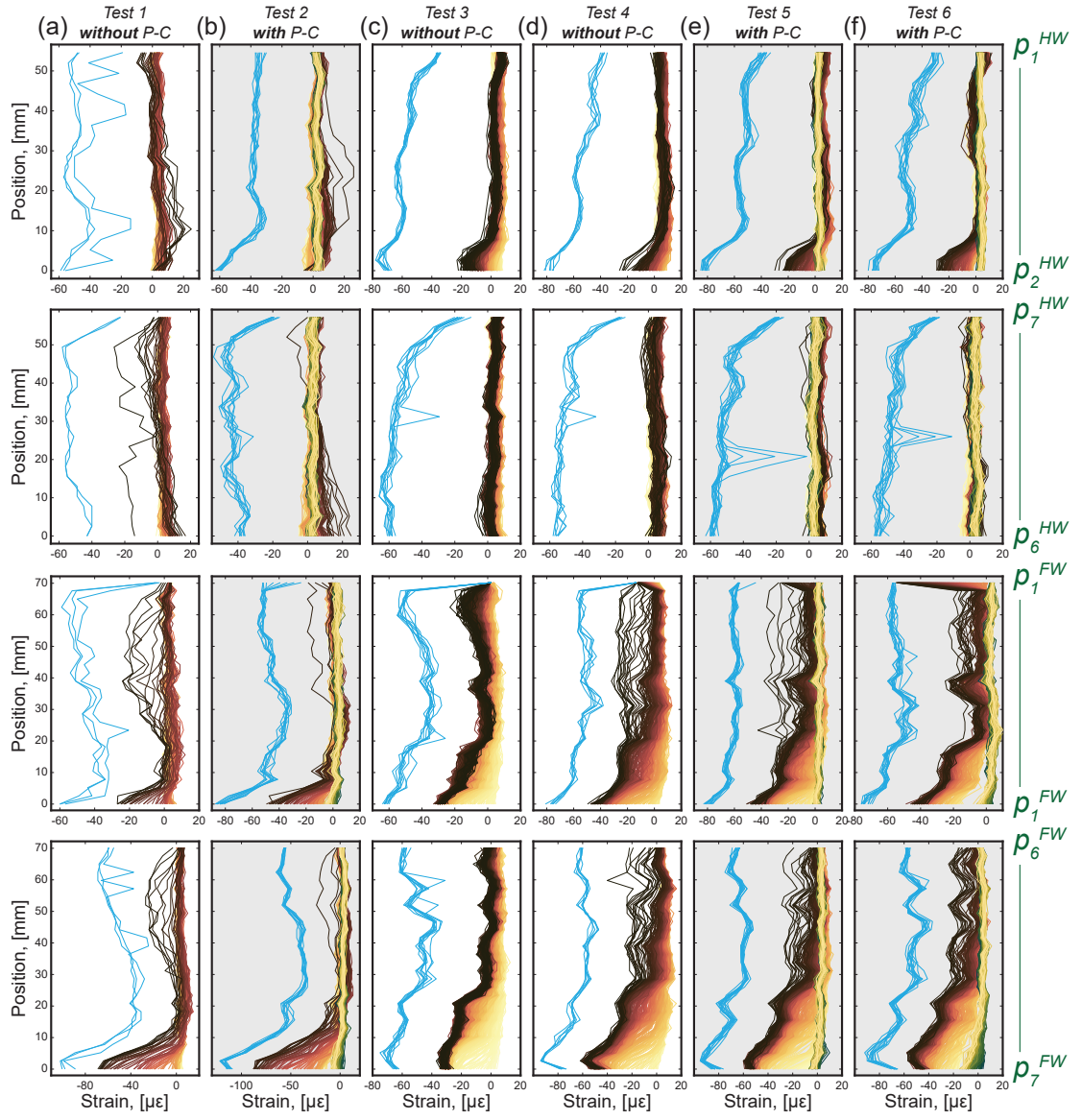


Fig. S7 (a)-(f) Distributed axial strain measurements along the fiber segments $P_1^{HW} \to P_2^{HW}$ (first row), $P_6^{HW} \to P_7^{HW}$ (second row), $P_1^{FW} \to P_2^{FW}$ (third row) and $P_6^{FW} \to P_7^{FW}$ (fourth row) for the Test 1-Test 6, respectively. For visualization purposes, only one of ten measurements is visualized. The orientation of the segments in this figure reflects the actual orientation of the fibers attached to the sample. The colorbars indicate the time in the specific test and refer to the ones displayed in Figs. 2a-f of the main manuscript. The light blue lines indicate the measurements retrieved after the observed stick-slip events. Tests involving fluid pre-conditioning (P-C) are indicated by a grey background.

The axial strain measurements retrieved in the FW show higher levels of deformation with respect to the fiber segments in the HW. As the injection protocols started, we generally observe relative extension in the lower portion of the axial segments of the FW (i.e., close to points P_1^{FW} and P_7^{FW}). We see that the lower the measurement point, the degree of relative extension detected is higher. This behavior is also partially observed in the HW, with the lower measurement points showing more extension. In the last few seconds (i.e., <5 to 10 seconds) before the stick-slip events, we observe precursory, accelerated deformation close to the segment points P_2^{FW} and P_6^{FW} in the FW, i.e., in the regions that are closer to the fault. Precursory, accelerated deformation is also observed in the proximity of the fault in the HW (segment points P_2^{HW} and P_6^{HW}) but it is not as prominent when compared to the deformation of the FW. We note that accelerated deformation is always expressed as a relative extensional process in the FW, whereas it is observed as both a relative compressional and extensional process in the FW. In comparison to the fault-parallel DSS measurements (see Fig. 3 of the main manuscript), we do not observe differences in the deformation induced by the pre-conditioning phase in the axial measurements. The only exception is found for Test 6 in the FW (third and fourth rows of Fig. S7f), where we observe that the bottom of the sample extends slightly more with respect to the rest of it. However, the level of relative extension at which we observe the stick-slip events does not seem to vary significantly with or without the pre-conditioning phase.

During the the acceleration phase observed shortly prior to the stick-slip events Latour et al. (2013), the DSS measurements of the axial lines in the FW (Fig. S7) show an extension front that unlocks from the bottom and quickly propagates upwards towards the fault. This potentially indicates that the stress imposed on the bottom half of the sample is released sequentially from the bottom upwards. The axial strain measurements of the HW show less heterogeneities and accelerated deformation but we can observe relative extension at the bottom of a majority of the segments possibly due to the dilation caused by the increase in the injection pressure to its maximum value. All the fiber segments show that the sample is arrested in a state of higher relative extension (light blue lines in Fig. S7), which is explained by the stress releases caused in response to the stick-slip events.

8 Localization of the Acoustic Emissions

Figure S8 shows the AE locations detected during the six reactivation tests (protocols provided in Fig. 2 of the main manuscript). In all the six tests we are able to localize the mainshock (Figs. S8b, c, d, f, g and h), whereas in $Test\ 1$ and $Test\ 4$ we also localize a foreshock (Figs. S8a and e). All the AEs are localized with an accuracy of at least ± 8 mm.

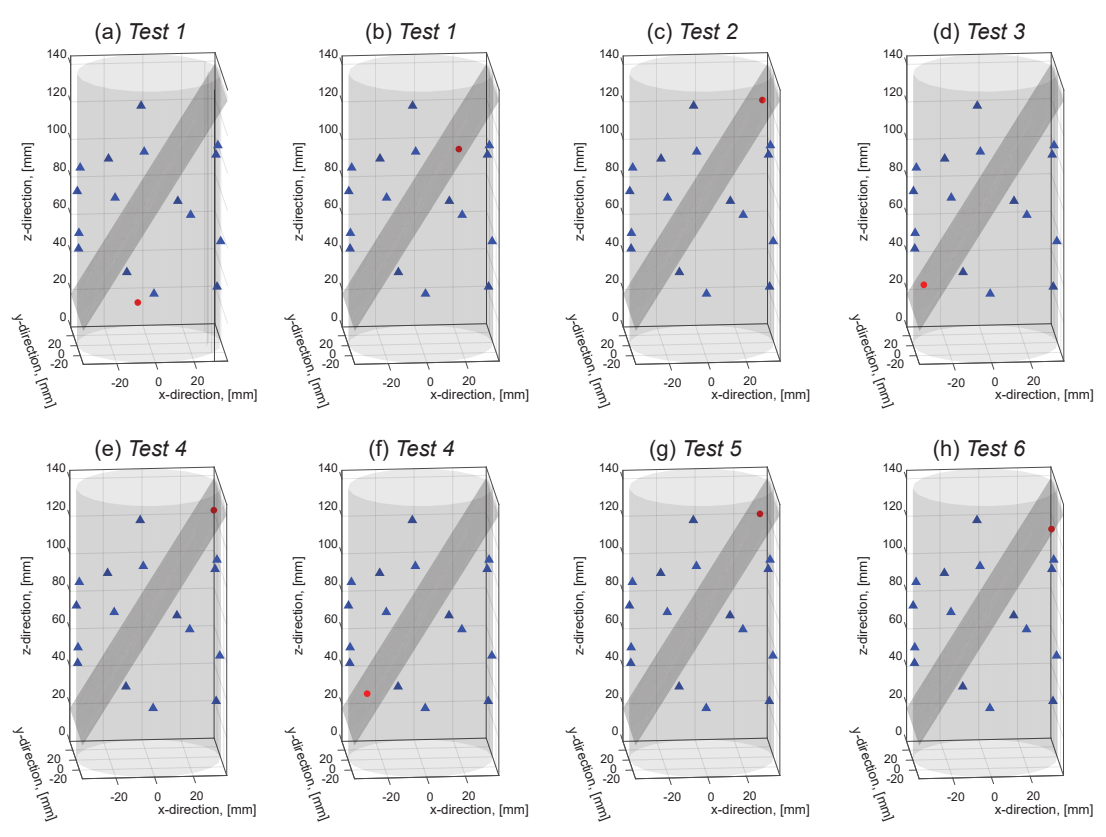


Fig. S8 AE locations (red dots) within the sample. The blue triangles indicate the PZT sensor positions. (a) A foreshock of *Test 1*, (b) the mainshock of *Test 2*, (d) the mainshock of *Test 3*, (e) a foreshock of *Test 4*, (f) the mainshock of *Test 4*, (g) the mainshock of *Test 5* and (h) the mainshock of *Test 6*.

9 Extended Mechanical Data Set

Figure S9 shows additional mechanical parameters determined during the dry failure envelope tests presented in the Supplementary Material 2 as a function of the applied confining pressure. For each observed stickslip event, we determine the peak strength τ_p (i.e., the value right before the stress drop, Fig. S9a), the residual strength τ_r (i.e., the value right after the stress drop, Fig. S9b) and the strength drop $\Delta \tau$ (Fig. S9c). Similarly, we track the evolution of the apparent friction τ/σ_N at the peak (Fig. S9d), residual (Fig. S9e) and the drop of it (Fig. S9f). The slip ΔS (Fig. S9g) is used to determine the scalar seismic moment M_0 (Fig. S9h) of each stick-slip event. Finally, we determine the moment magnitude associated to each event as $M_w = 2/3 \cdot (\log_{10}(M_0)-9.1)$ (Fig. S9i) (Hanks and Kanamori, 1979). We note that the values of M_0 and M_w are high for laboratory events. However, this overestimation is expected in such laboratory settings and is due to the boundary condition imposed on the sample (i.e., absence of an intact rock formation hosting the fault).

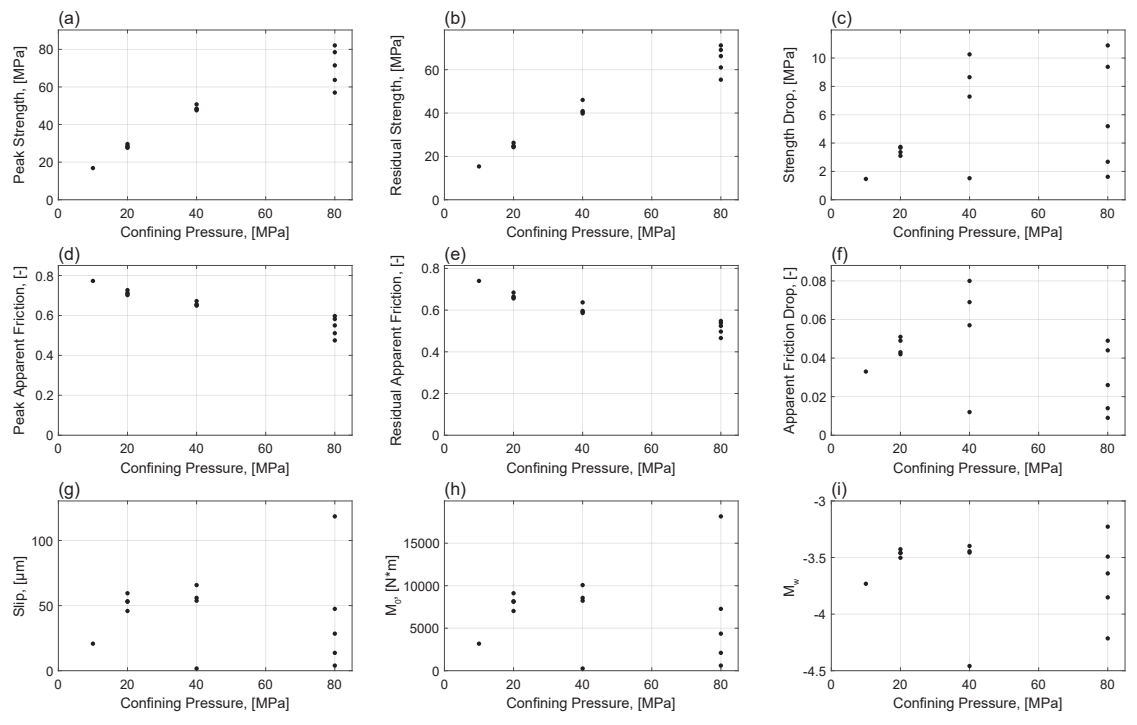


Fig. S9 Extended mechanical data set as a function of the confining pressure. (a) Peak strength, (b) residual strength, (c) strength drop, (d) peak apparent friction, (e) residual apparent friction, (f) apparent friction drop, (g) slip, (h) scalar seismic moment and (i) moment magnitude.

References

- Salazar Vásquez, A., Selvadurai, P.A., Bianchi, P., Madonna, C., Germanovich, L.N., Puzrin, A.M., Wiemer, S., Giardini, D., Rabaiotti, C.: Aseismic strain localization prior to failure and associated seismicity in crystalline rock. Scientific Reports (2024)
- Scholz, C.H.: The Mechanics of Earthquakes and Faulting, 3rd edn. Cambridge University Press, ??? (2019). https://doi.org/10.1017/9781316681473
- Selvadurai, P.A., Glaser, S.D., Parker, J.M.: On factors controlling precursor slip fronts in the laboratory and their relation to slow slip events in nature. Geophysical Research Letters 44(6), 2743–2754 (2017) https://doi.org/10.1002/2017GL072538
- Paterson, M.S., Wong, T.-f.: Experimental Rock Deformation: the Brittle Field vol. 348. Springer, ??? (2005)
- Witherspoon, P.A., Wang, J.S.Y., Iwai, K., Gale, J.E.: Validity of cubic law for fluid flow in a deformable rock fracture. Water Resources Research 16(6), 1016–1024 (1980) https://doi.org/10.1029/WR016i006p01016
- Zimmerman, R.W., Bodvarsson, G.S.: Hydraulic conductivity of rock fractures. Transport in Porous Media 23, 1–30 (1996) https://doi.org/10.1007/BF00145263
- Ye, Z., Ghassemi, A.: Injection-induced shear slip and permeability enhancement in granite fractures. Journal of Geophysical Research: Solid Earth 123(10), 9009–9032 (2018) https://doi.org/10.1029/2018JB016045
- Huo, J., Selvadurai, A.P.S., Meguid, M.: Permeability evolution in a fracture in granite during isotropic compression. Rock Mechanics and Rock Engineering (2024) https://doi.org/10.1007/s00603-024-03875-w
- Latour, S., Schubnel, A., Nielsen, S., Madariaga, R., Vinciguerra, S.: Characterization of nucleation during laboratory earthquakes. Geophysical Research Letters **40**(19), 5064–5069 (2013) https://doi.org/10.1002/grl.50974
- Hanks, T.C., Kanamori, H.: A moment magnitude scale. Journal of Geophysical Research: Solid Earth 84(B5), 2348–2350 (1979) https://doi.org/10.1029/JB084iB05p02348